THE JOURNAL OF PHYSICAL CHEMISTRY B

Article

Rab11 and Lysotracker Markers Reveal Correlation between Endosomal Pathways and Transfection Efficiency of Surface-Functionalized Cationic Liposome–DNA Nanoparticles

Ramsey N. Majzoub, Emily Wonder, Kai K Ewert, Venkata Ramana Kotamraju, Tambet Teesalu, and Cyrus R Safinya

J. Phys. Chem. B, **Just Accepted Manuscript** • DOI: 10.1021/acs.jpcb.6b04441 • Publication Date (Web): 20 May 2016

Rab11 and Lysotracker Markers Reveal Correlation between Endosomal Pathways and Transfection Efficiency of Surface-Functionalized Cationic Liposome–DNA Nanoparticles

Ramsey N. Majzoub,[a,b] Emily Wonder,[a] Kai K. Ewert,[a] Venkata Ramana Kotamraju,[c] Tambet Teesalu,[c,d,e] Cyrus R. Safinya[a]*

[a] Physics Department, Materials Department, and Molecular, Cellular and Developmental Biology Department, University of California, Santa Barbara, California 93106, United States of America

[b] Current address: Janssen Research & Development LLC, Spring House, Pennsylvania 19477, United States of America

[c] Cancer Research Center, Sanford Burnham Prebys Medical Discovery Institute, La Jolla, California 92037, United States of America

[d] Center for Nanomedicine and Department of Molecular, Cellular, and Developmental Biology, University of California, Santa Barbara, California 93106, United States of America

[e] Laboratory of Cancer Biology, Institute of Biomedicine and Translational Medicine, University of Tartu, Tartu 50411, Estonia

*Corresponding author contact information: safinya@mrl.ucsb.edu, 805-893 8635

Abstract

Cationic liposomes (CLs) are widely studied as carriers of DNA and short-interfering RNA for gene delivery and silencing, and related clinical trials are ongoing. Optimization of transfection efficiency (TE) requires understanding of CL–nucleic acid nanoparticle (NP) interactions with cells, NP endosomal pathways, endosomal escape, and events leading to release of active nucleic acid from the lipid carrier. Here, we studied endosomal pathways and TE of surface-functionalized CL–DNA NPs in PC-3 prostate cancer cells displaying over-expressed integrin and neuropilin-1 receptors. The NPs contained RGD-PEG-lipid or RPARPAR-PEG-lipid, targeting integrin and neuropilin-1 receptors, respectively, or control PEG-lipid. Fluorescence colocalization using Rab11-GFP and Lysotracker enabled simultaneous colocalization of NPs with recycling endosome (Rab11) and late endosome/lysosome (Rab7/Lysotracker) pathways at increasing mole fractions of pentavalent MVL5 (+5 *e*) at low (10 mol%), high (50 mol%), and very high (70 mol%) membrane charge density (σ_M). For these cationic NPs (lipid/DNA molar charge ratio, ρ_{chg} = 5), the influence of membrane charge density on pathway selection and transfection efficiency is similar for both peptide-PEG NPs, although, quantitatively, the effect is larger for RGD-PEG compared to RPARPAR-PEG NPs. At low σ_M, peptide-PEG NPs show preference for the recycling endosome over the late endosome/lysosome pathway. Increases in σ_M, from low to high, lead to decreases in colocalization with recycling endosomes and simultaneous increases in colocalization with the late endosome/lysosome pathway. Combining colocalization and functional TE data at low and high σ_M shows that higher TE correlates with a larger fraction of NPs colocalized with the late endosome/lysosome pathway while lower TE correlates with a larger fraction of NPs co-localized with the Rab11 recycling pathway. The findings lead to a hypothesis that increases in σ_M, leading to enhanced late endosome/lysosome pathway selection and higher TE, result from increased nonspecific electrostatic attractions between NPs and endosome luminal membranes, and conversely, enhanced recycling pathway for NPs and lower TE are due to weaker attractions. Surprisingly, at very high σ_M, the inverse relation between the two pathways observed at low and high σ_M breaks down, pointing to a more complex NP pathway behavior.

Introduction

Currently, an unprecedented level of research activity is centered on the delivery of nucleic acids with synthetic vectors (i.e., carriers) for the treatment of diseases stemming from misregulated or defective genes.[1–10] Numerous classes of synthetic vectors, including those based on lipids or polymers, are investigated as potential alternatives to engineered viral vectors for the delivery of therapeutic nucleic acids. While the vast majority of ongoing human gene therapy clinical trials targeting cancer, genetic, and infectious diseases employ engineered viral vectors,[1] the method suffers from safety issues typically not associated with synthetic vectors. Notably, use of engineered retroviral and adenoviral vectors has resulted in insertional mutagenesis leading to cancer in two patients treated for X-linked SCID (severe combined immunodeficiency) and in severe immune reactions resulting in two patient deaths, respectively.[11–13] The ease of tuning of the physicochemical properties of synthetic vectors makes them promising candidates for safe and controlled delivery of exogenous nucleic acids. The major challenge is improving their cell targeting and transfection efficiency properties, which are much inferior to those of viral vectors *in vivo*.[2–7]

Lipid-based drug delivery was first described soon after the discovery of liposomes by Bangham and Horne (Figure 1A, closed assemblies of lipid bilayers also called vesicles).[14] In these initial studies[15–17] researchers demonstrated the potential of liposomes as carriers of therapeutic drugs, proteins, and nucleic acids with hydrophobic and hydrophilic molecules encapsulated within the bilayer or aqueous interior, respectively.[18] Two challenges commonly encountered *in vivo* are insufficient circulation lifetime due to removal of carriers by immune cells and the lack of selectivity of therapeutic carriers towards the appropriate cell and tissue types.[19,20] The addition of PEG-lipids (PEG: poly(ethylene glycol)) to liposomes with the polymer chains in the brush state (e.g., 10 mol% for 2000 M_w PEG or 5 mol% for 5000 M_w PEG) improves colloidal stability of liposomes[21–23] and extends the circulation lifetime by preventing clearance by the mononuclear phagocytic system (Figure 1B).[24–28]

Felgner *et al.* developed a distinctly different DNA vector using cationic liposomes (CLs) in order to utilize the electrostatic attraction with anionic mammalian cells (i.e., due to sulfated proteoglycans at the cell surface).[29] The earlier work used anionic or neutral liposomes.[15–17] This initial landmark paper introducing "lipofection" (≈ 3500 citations to date) was followed by the demonstration of gene expression in targeted organs *in vivo*[30] and human clinical trials.[31] Later, synchrotron x-ray scattering studies showed that mixing cationic liposomes (CLs) with DNA leads to the spontaneous formation of collapsed CL–DNA condensates with distinct liquid crystalline phases. The most prevalent CL–DNA phase consists of a multilamellar structure, labeled L_α^C, with DNA monolayers sandwiched between cationic membranes (Figure 1C).[32,33] A change in the shape of the lipid molecules, resulting in changes to the spontaneous curvature of the membranes of CL–DNA complexes, revealed different structures including the inverted hexagonal structure (H_{II}^C), with DNA encapsulated within cationic lipid monolayer tubes,[34,35] and the H_I^C structure, with hexagonally ordered DNA rods surrounded by cylindrical micelles,[36]

which was achieved with custom-synthesized highly charged dendritic multivalent lipids (MVLs). Further studies with a series of multivalent lipids with charge between +2 *e* and +5 *e* led to the finding that membrane charge density (σ_M) is a predictive parameter for transfection by L_α^C CL–DNA complexes.[37,38] More recently, the structure of gyroid cubic phases of CL–short-interfering RNA (CL–siRNA) complexes have been quantitatively established by synchrotron X-ray diffraction. Owing to their saddle-shaped membranes that promote pore formation, cubic phase complexes are efficient at endosomal escape and gene silencing *in vitro*.[39,40]

It is noteworthy that an important advantage of cationic lipid vectors over engineered viral vectors is the ability to deliver very large pieces of DNA. This was first shown in the pioneering development of artificial human chromosomes, where extremely large pieces of DNA, of order 10^8 bps, were delivered into cells by lipofection.[41] CL–DNA vectors are self-assemblies of cationic liposomes and DNA,[35] which effectively removes limits on the length of the nucleic acid that may be complexed with membranes. Thus, synthetic vectors may be designed to carry full-length genes and regulatory sequences. In contrast, engineered viruses are limited in their DNA carrying capacity by their capsid size, and to date, only cDNA therapeutic genes (i.e., genes missing long noncoding introns) have been delivered. We should note that although natural capsids have relatively small nanometer scale sizes, very recent advances in our understanding of viral capsid protein assembly, both from the perspective of experiment and theory,[42–47] point to the possibility of future designs of significantly enlarged engineered capsids overcoming the current size limits.

Covalent attachment of targeting peptides or antibodies to the distal end of PEG-lipids (Figure 1C) promotes the delivery of therapeutic molecules to the cells positive for expression of the receptors of the affinity ligands.[19,20,48] Extended circulation lifetime due to steric stabilization of PEGylated CL–DNA nanoparticles (NPs),[49] coupled with targeting, can ensure localization of the systemically administered NP in the target tissue and cells. Similar ligand-PEG surface functionalization has been used with other delivery vehicles to promote kinesin transport and biomolecule capture.[50,51] However, numerous barriers remain, including uptake, endosomal escape, and therapeutic molecule release from the carrier. Previous work has shown that cellular uptake and therapeutic nucleic acid release can be improved by addition of targeting peptides and the incorporation of environmentally responsive materials that promote intracellular carrier disassembly, respectively.[52–55] However, designing PEGylated nanoparticles with efficient endosomal escape remains a significant challenge. One strategy is to chemically insert an acid-labile acylhydrazone bond between the lipid headgroup and the PEG chain (Figure 1C). A recent study has shown that the low pH ($\approx$ 5) of late endosomes induces dePEGylation,[56] which in turn leads to membrane charge density-promoted endosomal escape by activated fusion.[37,38]

Endocytosis of NP cargo by cells is typically followed by intracellular trafficking through one of two distinct pathways.[57] Figure 2 displays a schematic showing the roles of various Rab GTPases in early endosome, late endosome/lysosome, and recycling endosome trafficking. Rab proteins are a family of small GTPases in eukaryotes that coordinate intracellular vesicle

trafficking between organelles (i.e., budding of vesicular carriers from the donor membrane, followed by vesicle transport and fusion to the acceptor membrane).[58,59] Clathrin-coated pits (CCPs) and macropinocytic ruffles (MPRs) internalize extracellular medium and cargo into clathrin-coated vesicles (CCVs) and macropinosomes (MPs) that fuse, via Rab5, to form the early endosome (EE). (Rab5 coordinates vesicle budding, trafficking, and fusion between the plasma membrane and early endosomes.) Small, tubular vesicles containing Rab11 and/or Rab4 (not shown) bud from the early endosome and are recycled to the plasma membrane.[60] Alternatively, cargo from the EE can be trafficked to a large tubular structure called the perinuclear recycling center (PRC).[61] From the PRC, Rab11-positive spherical and tubular vesicles bud and recycle their cargo to the plasma membrane.[62,63] The fast and slow recycling pathways (i.e., directly from EE and through the PRC) allow cells to recycle receptors to the plasma membrane.[61] An alternate pathway to recycling is the late endosome/lysosome pathway. After sufficient time, the concentration of Rab5 on the EE membrane will decrease while the concentration of Rab7 increases.[64] Upon complete removal of Rab5, recycling events no longer occur and a new class of proteins associates with the vesicle.[65] This marks the transition into a late endosome/multivesicular body (LE/MVB). Aside from the formation of intraluminal vesicles (ILVs), the low pH of the LE/MVB distinguishes it from an EE.[65] Rab7 mediates fusion of LE/MVBs with lysosomes into hybrid lyso-endosomes, which contain characteristics of both LE/MVBs and lysosomes and mature into lysosomes after sufficient time.[66] Alternatively, LE/MVBs can fuse with the plasma membrane, resulting in the formation of exosomes through the release of ILVs.[67] A growing number of studies involving colocalization of NPs with endocytic markers have been published,[68–74] and one recent study has implicated recycling of lipid–siRNA NPs via exosome formation as a major bottleneck to siRNA delivery.[75]

In this study, we investigated the endosomal pathways and transfection efficiency (TE, a measure of expression of an exogenous gene that is transferred into the cell by the lipid carrier) of three types of surface-functionalized CL–DNA NPs with distinct coatings: control NPs containing PEG-lipid with no peptide, and NPs containing either RGD-PEG-lipid or RPARPAR-PEG-lipid (Figure 3).[76] Cryogenic transmission electron microscopy (TEM)[77] and dynamic light scattering (DLS) studies of PEGylated CL–DNA NPs[52] show that their diameter ranges between 100 nm and 150 nm. The linear RGD peptide used in this study (full peptide sequence: GRGDSP) targets integrin receptors (with $\alpha_5\beta_1$ as the preferred receptor). The RPARPAR peptide (a CendR sequence) binds to neuropilin-1. CendR peptides (sharing the carboxy-terminal consensus motif R/KXXR/K), of which RPARPAR is the prototypic example, have been shown to use a unique neuropilin-1-dependent internalization pathway that leads to cell uptake *in vitro* and extravasation/tissue penetration *in vivo*.[78–81] Prostate cancer (PC-3) cells displaying overexpressed integrins and neuropilin-1 were used as model human cancer cells.[82–85] The cationic liposomes consisted of mixtures of pentavalent MVL5 (+5 *e*),[37,86,87] neutral DOPC (1,2-dioleoyl-*sn*-glycero-3-phosphatidylcholine), and 10 mol% PEG2000-lipid with and without peptide attached at the distal end of PEG. Increases in the mol% of MVL5 in CLs allowed us to look for the effect of membrane charge density (σ_M, defined as total cationic charge divided by

the total membrane area) on CL–DNA NP endosomal pathway selection at low $\sigma_M \approx 0.0061$ e/Å^2 and high $\sigma_M \approx 0.021$ e/Å^2, corresponding to compositions of 10/80/10 and 50/40/10 for MVL5/DOPC/x in mol%, with x = PEG-lipid, RGD-PEG-lipid, or RPARPAR-PEG-lipid (see Materials and Methods). We further looked at NPs prepared at very high $\sigma_M \approx 0.025$ e/Å^2, corresponding to 70/20/10 for MVL5/DOPC/x. The cationic NPs were prepared at cationic lipid/DNA molar charge ratio $\rho_{chg} = 5$.

Previous optical fluorescence co-localization imaging using Rab5-GFP and a mutant form of Rab5 revealed that linear RGD-tagged and untagged PEGylated CL–DNA NPs enter the cell via endocytosis, leading to NP entrapment inside early endosomes.[68] To better understand how NP composition influences downstream endosomal pathways, and thus transfection efficiency after endocytosis, we developed a quantitative multi-organelle fluorescence colocalization method using Rab11-GFP and Lysotracker (an acidic organelle marker, which colocalizes with Rab7) that allowed us to simultaneously observe recycling endosomes (Rab11), late endosomes/lysosomes (Lysotracker), and fluorescently-labeled NPs. Significantly, while NPs utilize both pathways, we find that membrane charge density modulates the selection of pathways. Furthermore, while the trend for pathway selection at different σ_M is similar for RGD-PEG and RPARPAR-PEG NPs, the effect is larger for RGD-PEG NPs. At low σ_M, peptide-PEG NPs show preferred colocalization with Rab11 (recycling endosomes) compared to Lysotracker (late endosomes/lysosomes). For both peptide-PEG NPs, overall Rab11 colocalization decreases with increases in the NP's membrane charge density between low and high σ_M. The decrease in Rab11 colocalization coincides with an increase with Lysotracker colocalization. This finding suggests that increased electrostatic binding of NPs to endosome luminal membranes with increasing σ_M favors the late endosome/lysosome pathway. The behavior at very high σ_M is unexpected: here, peptide-PEG NPs show decreased colocalization with acidic organelles compared to high σ_M NPs (reverse of the trend between low and high σ_M) while colocalization with recycling endosomes remains roughly the same. As expected, the control PEG NPs show small but consistent increases in colocalization with the late endosome/lysosome pathway with increasing σ_M, most likely due to the aforementioned increase in nonspecific electrostatic attraction between NPs and luminal membranes of the endosome.

Transfection efficiency measurements of surface-functionalized CL–DNA NPs revealed improvement with increasing σ_M. RGD-PEG and PEG coated NPs showed the largest variations in TE, increasing by more than an order of magnitude between low and very high σ_M. In contrast, RPARPAR-PEG coated NPs showed more modest increases in TE by about a factor of four. Combining colocalization and TE data as a function of σ_M leads to the qualitative finding that an increase in TE correlates with a decrease in the fraction of NPs colocalized with the Rab11 recycling pathway and an increase in the fraction of NPs co-localized with Lysotracker along the late endosome/lysosome pathway.

Materials and Methods

Materials. DOPC was purchased from Avanti Polar Lipids as a solution in chloroform. Pentavalent MVL5,[88] PEG2000-lipid,[26] RGD-PEG2000-lipid, and RPARPAR-PEG2000-lipid[76] were synthesized as previously described. The pGL3 and pGFP plasmids encoding the luciferase and GFP genes were purchased from Promega, and several Rab-GFP plasmids (Rab7,[89] Rab9, and Rab11[90]) were purchased from addgene.org. Rab5-GFP plasmid was a gift from the Weimbs lab (Molecular, Cellular, and Developmental Biology Department, UCSB). All plasmids were propagated in *Escherichia coli* and purified using Qiagen Giga or Mega Prep kits. For microscopy studies, the pGFP plasmid was labeled using the Mirus Bio *Label* IT Nucleic Acid Labeling Kit with Cy5 (excitation/emission maximum: 649 nm/670 nm). Poly-L-lysine (Sigma-Aldrich) was used to coat glass slides prior to seeding cells for microscopy studies.

Liposome and DNA preparation. Stock solutions of MVL5 and PEG2000-lipid were prepared by dissolving them in a 3:1 chloroform:methanol mixture. RGD-PEG2000-lipid and RPARPAR-PEG2000-lipid were dissolved in a 65:23:2 chloroform:methanol:dH_20 (dH_20: deionized water) mixture. Lipids were combined at the desired molar ratio (all compositions investigated had either 10, 50 or 70 mol% MVL5 and 10 mol% RGD-PEG2000-, RPARPAR-PEG2000- or PEG2000-lipid; see Figure 3). After mixing the desired molar ratios, the organic solvent was evaporated by a stream of nitrogen followed by overnight (12–16 h) incubation in a vacuum. The appropriate amount of high resistivity water (18.2 MΩcm) was added to the dried lipid film to achieve the desired liposome concentration (0.5–2.0 mM). Hydrated films were incubated overnight at 37 °C to form liposomes. The liposome solution was then sonicated using a tip sonicator to promote the formation of small unilamellar vesicles. Following plasmid purification according the manufacturers protocol, pGFP was labeled using Cy5 according to the manufacturer's protocol with one modification: the incubation time at 37 °C was increased from 1 h to 2 h to improve labeling efficiency. When the unilamellar vesicles are mixed with Cy5-labeled DNA, they will self-assemble into fluorescent multilamellar nanoparticles.[91]

Membrane charge density. The membrane charge density can be calculated from the equation $\sigma_M = [1- \Phi_{nl}/(\Phi_{nl} + r\Phi_{cl})]\sigma_{cl}$.[37] Here, $r = A_{cl}/A_{nl}$ is the ratio of the headgroup areas of the cationic and the neutral lipid; $\sigma_{cl} = eZ/A_{cl}$ is the charge density of the cationic lipid with valence Z; Φ_{nl} and Φ_{cl} are the mole fractions of the neutral and cationic lipids, respectively. In the calculation, the neutral lipid component consists of the sum of DOPC and the PEG-lipid (with and without peptide). The membrane charge density was calculated using $A_{nl} = 72$ Å^2, $r_{MVL5} = 2.3$, and $Z_{MVL5} = 5.0$.[37] For the three compositions used in this study (10/80/10, 50/40/10, 70/20/10 molar ratio of MVL5/DOPC/x, with x = PEG-lipid, RGD-PEG-lipid, or RPARPAR-PEG-lipid), the membrane charge densities were low $\sigma_M \approx 0.0061$ e/Å^2 for 10/80/10, high $\sigma_M \approx 0.021$ e/Å^2 for 50/40/10, and very high $\sigma_M \approx 0.025$ e/Å^2 for 70/20/10. The nanoparticles studied were prepared at cationic lipid/DNA molar charge ratio (ρ_{chg}) = 5.

Cell culture and transfection. PC-3 cells (ATCC number: CRL-1435; human prostate cancer) were cultured in DMEM (Invitrogen) supplemented with 10% fetal bovine serum

(Gibco) and 1% Penicillin/Streptomycin (Invitrogen). Cells were passaged every 72 h to maintain subconfluency and kept in an incubator at 37 °C in a humidified atmosphere containing 5% CO_2. For transfection studies, cells were seeded in 24-well plates at 40,000 cells/well. CL–DNA NPs were prepared by diluting 1 μg of DNA and the appropriate amount of liposome solution (based on desired charge ratio and stock lipid concentration) to 250 μL in serum-free medium. After the mixing of lipid and DNA solutions, the NPs were incubated at room temperature for 20 min prior to their addition to cells. The cells were washed with PBS, and 200 μL of complex solution (containing 0.4 μg of DNA) was added to each well. The cells were incubated with the nanoparticle solution for 6 h. After 6 h, the NP solution was removed, the cells were washed with PBS, and fresh serum-containing medium was added. Cells were further incubated in the presence of serum-containing medium for 20–24 h. After the overnight incubation, cells were washed twice with PBS and then lysed and harvested with 150 μL of Passive Lysis Buffer (Promega). Further lysis was achieved by subjecting the lysate to one freeze-thaw cycle. Luciferase expression was measured using the Luciferase Assay System (Promega) and a Perkin-Elmer 1420 Victor3 V multilabel counter following the assay manufacturer's instructions and normalized to total cellular protein as measured with a Bradford Assay (BioRad). Measurements were performed in duplicate with error bars indicating the standard deviation. All data points were measured at least two times to ensure reproducibility.

Microscopy of nanoparticle uptake in cultured cells. Prior to seeding cells, 22 x 22 mm No. 1.5 glass coverslips were coated with poly-L-lysine. PC-3 cells were seeded on the coated coverslips in 6-well plates such that the confluency was 60–80% 24 h after seeding. At 24 h post-seeding, complexes were formed by mixing 10 μL of Lipofectamine 2000 (Life Technologies) with either 4 μg of the desired Rab-GFP plasmid (Rab11-GFP) or 2 μg of the desired Rab-GFP plasmid (Rab5-, Rab7-, and Rab9-GFP) and 2 μg of noncoding calf thymus DNA. The concentration of Rab5-, Rab7- and Rab9-GFP was reduced via substitution of calf thymus DNA to prevent overexpression of Rab proteins. Lipofectamine 2000/pRab-GFP complexes were added to cells in serum-free medium and removed 6 hours later, according to the manufacturer's protocol. After removal of the Lipofectamine complexes, cells were washed with PBS and incubated in serum-containing medium overnight. The next day, cells were washed and serum-containing medium was added again. Forty-eight hours after transfection, fluorescently-labeled NPs were prepared by mixing 2.4 μg of unlabeled pGFP with 0.6 μg of Cy5-labelled pGFP to produce a solution of 3 μg DNA in 250 μL of serum-free medium. The appropriate amount of liposome solution (based on charge ratio and stock lipid concentration) was diluted to 250 μL in serum-free DMEM. Liposome and DNA solutions were mixed together and incubated at room temperature for 20 min. The 6-well plates containing seeded coverslips were removed from the incubator, washed once with PBS, and 2 mL of serum-free medium was added to each well containing cells. The 500 μL of NP suspension was added to each well and cells were placed in the incubator for 4.5 h. After 4.5 hours, cells were removed and rinsed once with PBS. Following PBS washing, 2 mL of serum-free medium containing 50 ng/mL of LysoTracker® Red (Life Technologies) was added to each well. Cells were incubated at 37 °C for 30 min in the

presence of Lysotracker Red to allow for labeling of acidic organelles. After acidic organelle labeling, cells were washed two times with PBS and fixed using a PBS solution containing 3.7% formaldehyde. Cells were incubated in the presence of formaldehyde for 10 minutes at room temperature with occasional agitation. After fixation, cells were washed with PBS three times and mounted onto slides using Anti-fade mounting medium (Life Technologies). The anti-fade medium was cured overnight and coverslips were sealed to the glass slides using a fast-curing epoxy resin.

Cells were imaged within 5 days of fixation using an Olympus DSU microscope equipped with a 100× UPlanSApo objective, a Hamamatsu ImagEM CCD camera, and Metamorph software. Representative cells were chosen and imaged at z-steps of 1 μm. Prior to colocalization analysis, images were processed as follows. First, the z-stacks were deconvolved using the ImageJ plug-in Iterative Deconvolve 3D. Post-deconvolution processing consisted of a background subtraction with a 10-pixel rolling ball radius as well as a smooth filter for improved image clarity. Colocalization analysis was performed using custom-written Matlab routines and is described below.

Object-based quantitative colocalization analysis. Colocalization analysis[52,56,68,92] was performed on approximately 20–30 cells per NP composition. A rough outline of each cell was generated from an image produced by subtracting the NP channel from a saturated image of the Rab channel. This subtraction step allows automatic location of the cell boundary while excluding extracellular NPs, which form a thick fluorescent coat on the outside of the plasma membrane.[93]The Matlab routine prompts the user to mask neighboring cells in close proximity to the cell of interest and to set the bottom and top slice of each cell. For our analysis, we selected z-stack regions that were 2–3 μm thick. For each slice, NPs were located using a Matlab version of the algorithm first reported by Crocker and Grier.[94] Next, particles were given z-coordinates based on their brightness in each stack (some NPs can be imaged in more than one stack). Following the generation of a list of acidic organelle, recycling endosome, and NP coordinates, NPs were counted as colocalized with a marker (e.g., Lysotracker) if they were within three pixels of that marker and at least five pixels away from the other marker (e.g., Rab11-GFP). We refer to this method of colocalization as "object-based".[92] In all samples measured, a small fraction of NPs (< 18 %) were found to colocalize with both markers (data not shown). NPs were not designated any colocalization if they were at least five pixels away from both markers. The colocalization statistics were calculated by dividing the total number of colocalized NPs by the total number of intracellular NPs. This method for averaging, as opposed to single-cell statistical averaging, is analogous to how TE is measured with luciferase. (Luciferase expression measurements lack single-cell statistic due to cell lysis during harvesting.) Error for colocalization fractions is estimated at ±2%, as found for one sample that was imaged and analyzed twice.

Results

Transfection efficiency of MVL5-based CL–DNA nanoparticles. Figure 4 shows transfection efficiency (TE) as a function of mol% cationic lipid (MVL5) for CL–DNA NPs functionalized with PEG, RGD-PEG, and RPARPAR-PEG. The NPs were formed from CLs with MVL5/DOPC/x compositions equal to 10/80/10, 50/40/10, and 70/40/10 at the cationic lipid/DNA molar charge ratio (ρ_{chg}) = 5 (x = PEG-lipid, RGD-PEG-lipid, or RPARPAR-PEG-lipid). The TE of NPs increases with σ_M, with the exception of very high σ_M RGD-PEG NPs. At all σ_M, the transfection of RGD-PEG NPs is the highest, followed by the control PEG NPs. RPARPAR-PEG NPs had the lowest TE at every σ_M examined in this study. Furthermore, while TE increased by a little over an order of magnitude for RGD-PEG and PEG NPs between 10 mol% MVL5 and 50 mol% MVL5, the increase with RPARPAR NPs was more modest, about a factor of 4.

Lysotracker as a marker of acidic endocytic organelles. As shown in Figure 2, different members of the Rab family of GTPases are associated with different stages of the endocytic pathway. Figure 5A-D shows fluorescence micrographs of cells expressing the indicated Rab (marking distinct endosomes) and having acidic organelles fluorescently labeled by Lysotracker (a small, membrane-permeable dye that nonspecifically labels low-pH late endosomes and lysosomes). The micrographs indicate that Lysotracker shows little colocalization with Rab5 and Rab11 (Fig. 5A, B, markers of early and recycling endosomes, respectively), while showing high and moderate levels of colocalization with Rab7 (Fig. 5C, marker of late endosomes and lysosomes) and Rab9 (Fig. 5D, marker of late endosomes). The results of our quantitative colocalization analysis between Rabs 5, 11, 7, and 9 and Lysotracker are shown in Fig. 5E. The green region of each bar graph represents the fraction of Rab-labeled vesicles that lack Lysotracker colocalization (green signal in Fig. 5A-D) while the yellow region of the bar graph represents the fraction of Rab-labeled vesicles that do colocalize with Lysotracker (yellow due to overlap of green and red in Figure 5A-D). Rab5 and Rab11 show low levels of colocalization, likely due the finite spatial resolution of our images. Rab7 shows high levels of colocalization while the fraction of the total Rab9 labelled vesicles colocalized with Lysotracker is relatively low. A closer inspection of the data (and micrographs) reveals that this is not due to a low number of Rab9-Lysotracker colocalization events (yellow signal in micrographs) but instead due to the high number of Rab9 vesicles lacking Lysotracker colocalization (green signal in micrograph, green region of bar). This most likely arises because Rab9 marks other, nonendosomal organelles. In particular, Rab9 is known to mediate trafficking between late endosomes and the trans-Golgi network (Fig. 2).[32] The significant colocalization of Lysotracker with Rab7 and Rab9 confirms its usefulness as a marker of the late endosome/lysosome pathway.

Surface-functionalized CL–DNA NPs traffic through late endosome/lysosome and recycling pathways. Figure 6A shows a fluorescent micrograph of a PC-3 cell that has been incubated with CL–DNA NPs at low $\sigma_M \approx 0.0061$ e/Å^2 with a lipid molar ratio of 10/80/10 MVL5/DOPC/RPARPAR-PEG2K-lipid at ρ_{chg} = 5 for 5 hours. The NPs are fluorescently-

labeled (blue signal) by forming them with a mixture of Cy5-labeled and unlabeled DNA at a ratio of 20:80. The acidic organelles (red signal) are fluorescently labeled using Lysotracker-Red while recycling endosomes are labeled using transient expression of Rab11-GFP (green). The inset shows the corresponding bright field image. The boxed regions in Fig. 6A are magnified in Fig. 6B and C for clarity, and Fig. 6D-F displays single channel images of the region depicted in Fig. 6C, showing red (Lysotracker), green (Rab11-GFP), and blue (NP Cy5-DNA) channels. Fig. 6B contains a purple spot (i) and a cyan spot (ii) (see corresponding intensity profile in Fig. 6G) that exemplify how within a single cell, individual NPs can use either the late endosome/lysosome pathway (overlap of red and blue) or recycling pathway (overlap of green and blue). Fig. 6C and the corresponding intensity profile in Fig. 6H show a large green structure (green arrow in Fig. 6E and Fig. 6H) containing a high local concentration of Rab11-GFP. The high level of Rab11 and perinuclear position suggests that this structure is the perinuclear recycling center (PRC, see Fig. 2) where Rab11-labeled recycling endosomes are generated. This large Rab11-positive structure was seen in nearly all the cells visualized over the course of the investigation. The solid blue arrows in Fig. 6F and Fig. 6H highlight a Cy5-DNA-labeled NP which is inside the PRC. Furthermore, near the PRC is a large acidic organelle (red arrow in Fig. 6D and Fig. 6H) containing a NP (blue broken arrows in Fig. 6F and Fig. 6H). In summary, the three color fluorescence imaging of Rab11-GFP, Lysotracker-Red, and DNA-Cy5 allows simultaneous visualization of NPs within the recycling and late endosome/lysosome pathways. Moreover, there is not a high level of specificity in regards to the intracellular pathway of CL–DNA NPs (i.e., within single cells, NPs can be found in either pathway). These results suggest that a comprehensive study of NP uptake pathways requires quantitative colocalization for measuring the fraction of NPs using either the late endosome/lysosome or recycling pathway.

Low membrane charge density RPARPAR-PEG and RGD-PEG NPs prefer the Rab11-mediated recycling pathway. Figure 7 shows colocalization data for NPs formed at low $\sigma_M \approx 0.0061$ e/Å^2 with lipid molar ratios of 10/80/10 MVL5/DOPC/x at $\rho_{chg} = 5$, where x is either PEG-lipid (NP1), RGD-PEG-lipid (NP2), or RPARPAR-PEG-lipid (NP3) (see Figure 3). Fig. 7A-C shows fluorescent micrographs of fixed PC-3 cells expressing Rab11-GFP (green), treated with Lysotracker-Red (red), and incubated in the presence of labeled Cy5-DNA containing NPs (blue) for 5 hours. The insets show the bright field images. The boxed regions in Fig. 7A-C are magnified in Fig. 7E-G for clarity. Fluorescent intensity profiles along the lines in each boxed region are shown in Fig. 7H-J. In all three cases, an example of Rab11-NP colocalization [(i), (iii), (vi)] and Lysotracker-NP colocalization is shown [(ii), (iv), (v)]. In Fig. 7D, the results of simultaneous colocalization quantification are shown. The total heights of the bars indicate the average number of NPs per cell, while the red and green regions of the bars show the fraction of intracellular NPs that colocalize with Lysotracker and Rab11-GFP, respectively. The average number of NPs per cell that lack colocalization with a marker is indicated by the blue region. The data show that at this low σ_M, the addition of either RGD (NP2) or RPARPAR (NP3) to the distal end of the PEG moiety increases the total uptake of NPs into cells relative to the control NPs with PEG alone (NP1). RGD-PEG and RPARPAR-PEG

NPs show a stronger preference for the recycling pathway than the control PEG NPs, with high degree of colocalization with Rab11 (31%, 29%) compared to relatively low levels of colocalization with Lysotracker (10%, 15%). Despite RGD-PEG and RPARPAR-PEG NPs using completely different receptors for endocytosis (integrin and neuropilin-1, respectively) they show similar colocalization statistics. The control PEG NPs show moderate colocalization with both markers. They have only a slight preference for the Rab11 pathway over the late endosome/lysosome pathway (22% and 17%, respectively).

High membrane charge density RPARPAR-PEG and PEG NPs show comparable preference for either pathway while RGD-PEG NPs prefer the late endosome/lysosome pathway. Figure 8 shows colocalization data for NPs formed at high $\sigma_M \approx 0.021$ e/Å^2 with lipid molar ratios of 50/40/10 MVL5/DOPC/x at ρ_{chg}=5, where x is either PEG-lipid (NP4), RGD-PEG-lipid (NP5), or RPARPAR-PEG-lipid (NP6) (see Figure 3). Fluorescent micrographs (Fig. 8A-C), magnified boxed regions (Fig. 8E-G), intensity profiles (Fig. 8H-J), and results of simultaneous colocalization quantification (Fig. 8D) are shown. Total NP uptake is overall lower compared to low σ_M formulations, with peptide-PEG NPs showing a larger reduction in uptake. RPARPAR-PEG NPs and control PEG NPs show nearly equal colocalization with both Rab11 and acidic organelles, with RPARPAR-PEG NPs showing higher slightly fractions along both pathways. In contrast, RGD-PEG NPs show Lysotracker colocalization (29%) moderately higher than Rab11 colocalization (21%).

Very high membrane charge density RGD-PEG and RPARPAR-PEG NPs show reduced preference for late endosome/lysosome pathway compared to recycling pathway. Figure 9 shows colocalization data for NPs formed at very high $\sigma_M \approx 0.025$ e/Å^2 with lipid molar ratios of 70/20/10 MVL5/DOPC/x at ρ_{chg}=5, where x is either PEG-lipid (NP7), RGD-PEG-lipid (NP8), or RPARPAR-PEG-lipid (NP9) (see Figure 3). Fluorescent micrographs (Fig. 9A-C), magnified boxed regions (Fig. 9E-G), intensity profiles (Fig. 9H-J), and results of simultaneous colocalization quantification (Fig. 9D) are shown. Total NP uptake is the reverse of what was seen for low-σ_M NP formulations: the control (PEG) NPs show the highest uptake, followed by RGD-PEG and then RPARPAR-PEG NPs. Between high and very high σ_M formulations, the uptake of control PEG NPs roughly doubled. While colocalization with Rab11 remained unchanged from that at high σ_M formulations for RGD-PEG and RPARPAR-PEG NPs, the fraction traveling along the late endosome/lysosome pathway is reduced, especially for RGD-PEG NPs (from 29% to 16%). The control PEG NPs show a slight preference for the late endosome/lysosome pathway over the Rab11 recycling pathway.

Discussion

The transfection efficiency results presented in Figure 4 are in agreement with previous work that found that the TE of PEGylated CL–DNA NPs, while significantly lower than that of CL–DNA complexes lacking PEG, increases with σ_M and/or RGD-tagging.[52] The low TE of

PEGylated NPs, at low membrane charge density in particular, has been attributed to their poor uptake and endosomal escape.[52,56] Peptide-tagging of PEGylated NPs improves their binding, subsequent uptake, and TE, although the effect of peptide-tagging on intracellular NP pathway selection is poorly understood. Previous work with univalent and multivalent CL–DNA complexes lacking the PEG coat found that membrane charge density modulates cell binding, internalization, endosomal escape, and transfection efficiency.[37,38] The linear RGD sequence used in this study binds to $\alpha_5\beta_1$ integrins, which has been previously implicated as a viable internalization pathway for ultimately achieving efficient transfection.[52] The TE of RGD-PEG MVL5-based NPs is much lower in the PC-3 cells investigated here than the mouse L-cells used in a previous study.[52] This finding is consistent with human cells typically being considered "hard-to-transfect." RPARPAR-PEG NPs, on the other hand, actually reduced TE relative to the control PEG NPs that lack peptides. RPARPAR, a CendR motif peptide that binds to the neuropilin-1 receptor, has shown excellent targeting and drug delivery properties *in vivo*.[78] The comparable uptake of RPARPAR-PEG NPs coupled with its low TE in the current study suggests that it uses a different trafficking pathway from RGD-PEG NPs that is not conducive to delivery of large plasmids.

Figure 10 summarizes the colocalization of the NP formulations with Rab11-labeled recycling endosomes and acidic organelles labeled with Lysotracker. Both Rab11 and Lysotracker colocalization show clear trends with increasing mol% MVL5 (i.e., increasing membrane charge density), regardless of the type of NP. The fraction of control (PEG) NPs colocalized with Rab11 recycling endosomes is nearly constant between low and very high σ_M ($\approx$ 22%, 19%), while the fraction colocalized with late endosomes/lysosomes increases slightly between low and very high σ_M (from 17% to 25%). The observation that the recycling pathway of PEG NPs is essentially independent of σ_M suggests that the sections of the early endosome membrane that pinch off in the recycling pathway (Fig. 3) either lack or have a very low concentration of anionic lipids, resulting in weak electrostatic interactions with the cationic PEG NPs. The peptide-PEG NPs show distinctly different behavior. At low σ_M (10 mol% MVL5), RGD-PEG and RPARPAR-PEG NPs show strong preference for the recycling pathway (31% and 29% colocalized with Rab11) compared to the late endosome/lysosome pathway (10%, 15% colocalized with Lysotracker). The increased recycling of peptide-PEG NPs compared to control NPs at low σ_M suggests that ligand-receptor interactions tend to drive NPs in early endosomes along Rab11-mediated recycling pathways. At high σ_M (50 mol% MVL5), with comparable fractions of NPs colocalized along either pathway, RGD-PEG and RPARPAR-PEG NPs show decreased recycling (21%, 24% colocalized with Rab11) and increased late endosome/lysosome pathway colocalization (29%, 25% colocalized with Lysotracker) compared to low σ_M NPs. The colocalization findings, in the low to high σ_M regime, lead to a hypothesis that increased nonspecific electrostatic attractions between the peptide-PEG coated NPs and the endosome luminal membrane, which is expected to occur with increases in σ_M,[37,52,56] increases the fraction

of NPs following the late endosome/lysosome pathway, thus decreasing the fraction along the recycling pathway.

At very high σ_M (70% MVL5), recycling of RGD-PEG and RPARPAR-PEG NPs remains nearly unchanged compared to that at high σ_M. In contrast, the peptide-PEG NPs show decreased colocalization of NPs along the late endosome/lysosome pathway. The combined effects of peptide-receptor binding and increased σ_M is expected to lead to more frequent collisions between cationic peptide-PEG NPs and the anionic luminal membrane of endosomes. This would result in a higher probability of membrane fusion, leading to endosomal escape and lower colocalization with acidic organelles. Overall, the lack of the inverse relation between the two pathways (as observed for peptide-PEG NPs at low and high σ_M) suggests a more complex pathway behavior at very high σ_M.

To obtain the relationship between pathway preferences and NP efficacy, transfection efficiency was plotted against NP colocalization with Rab11 (Fig. 11A) and Lysotracker (Fig. 11B) by combining TE and colocalization data (Fig. 4 and Fig. 10). The plots of TE versus pathway selection of NPs shows an inverse correlation between TE and NP colocalization with the Rab11 recycling pathway and a direct correlation between TE and NP colocalization with the late endosome/lysosome pathway (Lysotracker), independent of the type of NP. This suggests that unlike the Rab11-mediated recycling pathway, the late endosome/lysosome pathway allows time for endosomal escape and, subsequently, higher TE. Nevertheless, on closer inspection one can readily discern that RPARPAR-PEG and PEG data are clustered closer together compared to the RGD-PEG data, indicating that membrane charge density has a larger effect on pathway selection and transfection efficiency for RGD-PEG NPs. For example, Fig. 10 shows that between low and very high σ_M (10 and 70 mol% MLV5), RGD-PEG NPs show variations from 10% to 29% in colocalization with Lysotracker and from 31% to 21% in colocalization with Rab11. In comparison, RPARPAR-PEG NPs show a smaller variation in Lysotracker colocalization from 15% to 25% and an even more modest variation in Rab11 colocalization from 29% to 24%. For control (PEG) NPs, Lysotracker colocalization similarly show a modest change from 17% to 25% while changes in colocalization with Rab11 were minimal from 22% to 19%. These quantitative differences in pathway selection between the peptide-PEG NPs most likely arise from their binding to different cell receptors.

Conclusions

PEGylated CL–nucleic acid NPs with targeting peptides attached at the distal end of the PEG chain are promising carriers of therapeutic nucleic acids, but their intracellular trafficking along different endosomal pathways and eventual endosomal escape mechanisms are poorly understood. In this study, we investigated the uptake and trafficking properties of pentavalent MVL5 (+5 *e*) surface-functionalized CL–DNA NPs using a custom-developed multi-organelle fluorescence colocalization method. To understand the effect of membrane charge density on

transfection efficiency and endosomal pathway selection of surface-functionalized CL–DNA NPs, we investigated colocalization of PEG, RGD-PEG, and RPARPAR-PEG NPs with distinct endocytic markers (Rab11 for recycling endosome and Lysotracker for acidic organelles) at low, high, and very high membrane charge density (σ_M). Previous work has suggested that nanoparticles do use multiple pathways, but we present the first direct evidence of nanoparticles within a single cell simultaneously colocalized with both a recycling vesicle and a degradative vesicle. This behavior is in contrast to transferrin or LDL particles, which are recognized by the cell and trafficked solely through specific pathways.[95]

The key findings for RGD-PEG and RPARPAR-PEG NPs are as follows. At low σ_M, NPs exhibit low transfection efficiency (TE) and enhanced colocalization with Rab11-mediated recycling endosomes compared to late endosome/lysosome organelles. At high σ_M, NPs have significantly higher TE, decreased colocalization with recycling endosomes, and increased colocalization with late endosome/lysosome organelles. The NP colocalization behavior at very high σ_M shows a different trend where the fraction of NPs colocalized with recycling endosomes is unchanged even though the fraction of NPs colocalized with the late endosomes/lysosomes is reduced compared to that at high σ_M. The absence of the inverse relation between colocalization of NPs along the two pathways, seen at low and high σ_M, suggests a more complex pathway selection behavior at very high σ_M.

The observation of similar trends in endosomal pathway selection and transfection efficiency of both RGD-PEG and RPARPAR-PEG NPs at different σ_M is notable. This is because the current study focused on overall highly cationic NPs with the cationic lipid/DNA molar charge ratio of $\rho_{chg} = 5$, where nonspecific electrostatic interactions with cell components are significant. Future studies emphasizing specific ligand-receptor interactions over nonspecific electrostatic interactions, both at the plasma membrane surface and inside early endosomes, will require studies of NPs prepared near the isoelectric point where $\rho_{chg} = 1$. Finally, it is important to note that a significant fraction of NPs do not show colocalization with either of the investigated pathways, implying the NPs are involved in alternative pathways (e.g., Rab4-mediated recycling). These initial Rab-based colocalization studies open the path for future colocalization studies with other members of the Rab family that colocalize with a broader range of intracellular organelles. This would lead to a more comprehensive understanding of the influence of NP composition on pathway selection, yielding further insights for improving NP transfection efficiency.

Acknowledgment. We would like to acknowledge insightful discussions on peptide targeting motifs with Erkki Ruoslahti. This work was supported by the National Institute of Health under award GM-59288 (CRS), by Cancer Center Support Grant CA30199 from the National Cancer Institute, by Norwegian-Estonian collaboration grant EMP181 (TT), European Research Council starting grant GLIOMADDS from European Regional Development Fund (TT), and Wellcome

Trust International Fellowship WT095077MA (TT). The work was also supported in part by the National Science Foundation under award DMR-1401784 (CRS, automated image analysis of nanoparticles). The Rab5-GFP plasmid was a generous gift from the Weimbs Lab (UCSB). The Spinning Disk Microscopy was performed at the NRI-MCDB Microscopy Facility at UC Santa Barbara; we thank Mary Raven for her help. EW was supported by the National Science Foundation Graduate Research Fellowship under Grant No. DGE 1144085.

References

(1) Gene Therapy Clinical Trials Worldwide http://www.wiley.com/legacy/wileychi/genmed/clinical/ (accessed May 20, 2010).

(2) Guo, X.; Huang, L. Recent Advances in Nonviral Vectors for Gene Delivery. *Acc. Chem. Res.* **2012**, *45*, 971–979.

(3) Safinya, C. R.; Ewert, K. K.; Majzoub, R. N.; Leal, C. Cationic Liposome–nucleic Acid Complexes for Gene Delivery and Gene Silencing. *New J. Chem.* **2014**, *38*, 5164–5172.

(4) Yin, H.; Kanasty, R. L.; Eltoukhy, A. a; Vegas, A. J.; Dorkin, J. R.; Anderson, D. G. Non-Viral Vectors for Gene-Based Therapy. *Nat. Rev. Genet.* **2014**, *15*, 541–555.

(5) Sharma, V. D.; Ilies, M. A. Heterocyclic Cationic Gemini Surfactants: A Comparative Overview of Their Synthesis, Self-Assembling, Physicochemical, and Biological Properties. *Med. Res. Rev.* **2014**, *34*, 1–44.

(6) *Nucleic Acid Transfection*; Bielke, W., Erbacher, C., Eds.; Topics in current chemistry, Vol. 296; Springer: Berlin, 2010.

(7) Ewert, K. K.; Zidovska, A.; Ahmad, A.; Bouxsein, N. F.; Evans, H. M.; McAllister, C. S.; Samuel, C. E.; Safinya, C. R. Cationic Liposome-Nucleic Acid Complexes for Gene Delivery and Silencing: Pathways and Mechanisms for Plasmid DNA and siRNA. *Top. Curr. Chem.* **2010**, *296*, 191–226.

(8) *Non-Viral Vectors for Gene Therapy*, 2nd ed.; Huang, L., Hung, M.-C., Wagner, E., Eds.; Advances in Genetics, Vol. 53; Elsevier Academic Press: San Diego, 2005.

(9) Ewert, K. K.; Ahmad, A.; Evans, H. M.; Safinya, C. R. Cationic Lipid-DNA Complexes for Non-Viral Gene Therapy: Relating Supramolecular Structures to Cellular Pathways. *Expert Opin. Biol. Ther.* **2005**, *5*, 33–53.

(10) Jana, B.; Sarkar, J.; Mondal, P.; Barman, S.; Mohapatra, S.; Bhunia, D.; Pradhan, K.; Saha, A.; Adak, A.; Ghosh, S.; et al. A Short GC Rich DNA Derived from Microbial Origin Targets Tubulin/microtubules and Induces Apoptotic Death of Cancer Cells. *Chem. Commun.* **2015**, *51*, 12024–12027.

(11) Williams, D. A.; Baum, C. Gene Therapy - New Challenges Ahead. *Science* **2003**, *302*, 400–401.

(12) Thomas, C. E.; Ehrhardt, A.; Kay, M. A. Progress and Problems with the Use of Viral Vectors for Gene Therapy. *Nat. Rev. Genet.* **2003**, *4*, 346–358.

(13) Hacein-Bey-Abina, S.; Garrigue, A.; Wang, G. P.; Soulier, J.; Lim, A.; Morillon, E.; Clappier, E.; Caccavelli, L.; Delabesse, E.; Beldjord, K.; et al. Insertional Oncogenesis in 4 Patients after Retrovirus-Mediated Gene Therapy of SCID-X1. *J. Clin. Invest.* **2008**, *118*, 3132–3142.

(14) Bangham, A. D.; Horne, R. W. Negative Staining of Phospholipids and Their Structural Modification by Surface-Active Agents as Observed in the Electron Microscope. *J. Mol. Biol.* **1964**, *8*, 660–668.

(15) Gregoriadis, G.; Leathwood, P. D.; Ryman, B. E. Enzyme Entrapment in Liposomes. *FEBS Lett.* **1971**, *14*, 95–99.

(16) Gregoriadis, G.; Ryman, B. E. Fate of Protein-Containing Liposomes Injected into Rats. An Approach to the Treatment of Storage Diseases. *Eur. J. Biochem.* **1972**, *24*, 485–491.

(17) Gregoriadis, G. The Carrier Potential of Liposomes in Biology and Medicine Part I. *N. Engl. J. Med.* **1976**, *295*, 704–710.

(18) Safinya, C. R.; Ewert, K. K. Materials Chemistry: Liposomes Derived from Molecular Vases. *Nature* **2012**, *489*, 372–374.

(19) Immordino, M. L.; Dosio, F.; Cattel, L. Stealth Liposomes: Review of the Basic Science, Rationale, and Clinical Applications, Existing and Potential. *Int. J. Nanomedicine* **2006**, *1*, 297–315.
(20) Ruoslahti, E.; Bhatia, S. N.; Sailor, M. J. Targeting of Drugs and Nanoparticles to Tumors. *J. Cell Biol.* **2010**, *188*, 759–768.
(21) De Gennes, P.-G. *Scaling Concepts in Polymer Physics*, 1st ed.; Cornell University Press: New York, 1979.
(22) Needham, D.; McIntosh, T. J.; Lasic, D. D. Repulsive Interactions and Mechanical Stability of Polymer-Grafted Lipid Membranes. *Biochim. Biophys. Acta - Biomembr.* **1992**, *1108*, 40–48.
(23) Kuhl, T. L.; Leckband, D. E.; Lasic, D. D.; Israelachvili, J. N. Modulation of Interaction Forces between Bilayers Exposing Short-Chained Ethylene Oxide Headgroups. *Biophys. J.* **1994**, *66*, 1479–1488.
(24) Klibanov, A. L.; Maruyama, K.; Torchilin, V. P.; Huang, L. Amphipathic Polyethyleneglycols Effectively Prolong the Circulation Time of Liposomes. *FEBS Lett.* **1990**, *268*, 235–237.
(25) Blume, G.; Cevc, G. Liposomes for the Sustained Drug Release in Vivo. *Biochim. Biophys. Acta* **1990**, *1029*, 91–97.
(26) Papahadjopoulos, D.; Allen, T. M.; Gabizon, A.; Mayhew, E.; Matthay, K.; Huang, S. K.; Lee, K. D.; Woodle, M. C.; Lasic, D. D.; Redemann, C. Sterically Stabilized Liposomes: Improvements in Pharmacokinetics and Antitumor Therapeutic Efficacy. *Proc. Natl. Acad. Sci. U. S. A.* **1991**, *88*, 11460–11464.
(27) Allen, T. M.; Hansen, C.; Martin, F.; Redemann, C.; Yau-Young, A. Liposomes Containing Synthetic Lipid Derivatives of Poly(ethylene Glycol) Show Prolonged Circulation Half-Lives in Vivo. *Biochim. Biophys. Acta - Biomembr.* **1991**, *1066*, 29–36.
(28) Woodle, M. C.; Lasic, D. D. Sterically Stabilized Liposomes. *Biochim. Biophys. Acta* **1992**, *1113*, 171–199.
(29) Felgner, P. L.; Gadek, T. R.; Holm, M.; Roman, R.; Chan, H. W.; Wenz, M.; Northrop, J. P.; Ringold, G. M.; Danielsen, M. Lipofection: A Highly Efficient, Lipid-Mediated DNA-Transfection Procedure. *Proc. Natl. Acad. Sci. U. S. A.* **1987**, *84*, 7413–7417.
(30) Zhu, N.; Liggitt, D.; Liu, Y.; Debs, R. Systemic Gene Expression after Intravenous DNA Delivery into Adult Mice. *Science.* **1993**, *261*, 209–211.
(31) Nabel, G. J.; Nabel, E. G.; Yang, Z. Y.; Fox, B. A.; Plautz, G. E.; Gao, X.; Huang, L.; Shu, S.; Gordon, D.; Chang, A. E. Direct Gene Transfer with DNA-Liposome Complexes in Melanoma: Expression, Biologic Activity, and Lack of Toxicity in Humans. *Proc. Natl. Acad. Sci. U. S. A.* **1993**, *90*, 11307–11311.
(32) Rädler, J. O.; Koltover, I.; Salditt, T.; Safinya, C. R. Structure of DNA – Cationic Liposome Complexes : DNA Intercalation in Multilamellar Membranes in Distinct Interhelical Packing Regimes. *Science* **1997**, *275*, 810–814.
(33) Koltover, I.; Salditt, T.; Safinya, C. R. Phase Diagram, Stability, and Overcharging of Lamellar Cationic Lipid-DNA Self-Assembled Complexes. *Biophys. J.* **1999**, *77*, 915–924.
(34) Koltover, I.; Salditt, T.; Rädler, J. O.; Safinya, C. R. An Inverted Hexagonal Phase of Cationic Liposome-DNA Complexes Related to DNA Release and Delivery. *Science* **1998**, *281*, 78–81.
(35) Safinya, C. Structures of Lipid – DNA Complexes : Supramolecular Assembly and Gene

Delivery. *Curr. Opin. Struct. Biol.* **2001**, *11*, 440–448.
(36) Ewert, K. K.; Evans, H. M.; Zidovska, A.; Bouxsein, N. F.; Ahmad, A.; Safinya, C. R. A Columnar Phase of Dendritic Lipid-Based Cationic Liposome-DNA Complexes for Gene Delivery: Hexagonally Ordered Cylindrical Micelles Embedded in a DNA Honeycomb Lattice. *J. Am. Chem. Soc.* **2006**, *128*, 3998–4006.
(37) Ahmad, A.; Evans, H. M.; Ewert, K.; George, C. X.; Samuel, C. E.; Safinya, C. R. New Multivalent Cationic Lipids Reveal Bell Curve for Transfection Efficiency versus Membrane Charge Density: Lipid - DNA Complexes for Gene Delivery. *J. Gene Med.* **2005**, *7*, 739–748.
(38) Lin, A. J.; Slack, N. L.; Ahmad, A.; George, C. X.; Samuel, C. E.; Safinya, C. R. Three-Dimensional Imaging of Lipid Gene-Carriers: Membrane Charge Density Controls Universal Transfection Behavior in Lamellar Cationic Liposome-DNA Complexes. *Biophys. J.* **2003**, *84*, 3307–3316.
(39) Leal, C.; Bouxsein, N. F.; Ewert, K. K.; Safinya, C. R. Highly Efficient Gene Silencing Activity of siRNA Embedded in a Nanostructured Gyroid Cubic Lipid Matrix. *J. Am. Chem. Soc.* **2010**, *132*, 16841–16847.
(40) Leal, C.; Ewert, K. K.; Shirazi, R. S.; Bouxsein, N. F.; Safinya, C. R. Nanogyroids Incorporating Multivalent Lipids: Enhanced Membrane Charge Density and Pore Forming Ability for Gene Silencing. *Langmuir* **2011**, *27*, 7691–7697.
(41) Harrington, J. J.; Van Bokkelen, G.; Mays, R. W.; Gustashaw, K.; Willard, H. F. Formation of de Novo Centromeres and Construction of First-Generation Human Artificial Microchromosomes. *Nat. Genet.* **1997**, *15*, 345–355.
(42) Lavelle, L.; Gingery, M.; Phillips, M.; Gelbart, W. M.; Knobler, C. M.; Cadena-Nava, R. D.; Vega-Acosta, J. R.; Pinedo-Torres, L. A.; Ruiz-Garcia, J. Phase Diagram of Self-Assembled Viral Capsid Protein Polymorphs. *J. Phys. Chem. B* **2009**, *113*, 3813–3819.
(43) Prinsen, P.; Van Der Schoot, P.; Gelbart, W. M.; Knobler, C. M. Multishell Structures of Virus Coat Proteins. *J. Phys. Chem. B* **2010**, *114*, 5522–5533.
(44) Cadena-Nava, R. D.; Comas-Garcia, M.; Garmann, R. F.; Rao, A. L. N.; Knobler, C. M.; Gelbart, W. M. Self-Assembly of Viral Capsid Protein and RNA Molecules of Different Sizes: Requirement for a Specific High Protein/RNA Mass Ratio. *J. Virol.* **2011**, *86*, 3318–3326.
(45) Knobler, C. M.; Gelbart, W. M. Physical Chemistry of DNA Viruses. *Annu. Rev. Phys. Chem.* **2009**, *60*, 367–383.
(46) Gelbart, W. M.; Knobler, C. M. The Physics of Phages. *Phys. Today* **2008**, *61*, 42–47.
(47) Roos, W. H.; Bruinsma, R.; Wuite, G. J. L. Physical Virology. *Nat. Phys.* **2010**, *6*, 733–743.
(48) Peer, D.; Karp, J. M.; Hong, S.; Farokhzad, O. C.; Margalit, R.; Langer, R. Nanocarriers as an Emerging Platform for Cancer Therapy. *Nat. Nanotechnol.* **2007**, *2*, 751–760.
(49) Martin-Herranz, A.; Ahmad, A.; Evans, H. M.; Ewert, K.; Schulze, U.; Safinya, C. R. Surface Functionalized Cationic Lipid-DNA Complexes for Gene Delivery: PEGylated Lamellar Complexes Exhibit Distinct DNA-DNA Interaction Regimes. *Biophys. J.* **2004**, *86*, 1160–1168.
(50) Jana, B.; Biswas, A.; Mohapatra, S.; Saha, A.; Ghosh, S. Single Functionalized Graphene Oxide Reconstitutes Kinesin Mediated Intracellular Cargo Transport and Delivers Multiple Cytoskeleton Proteins and Therapeutic Molecules into the Cell. *Chem. Commun.* **2014**, *50*, 11595–11598.

(51) Jana, B.; Mondal, G.; Biswas, A.; Chakraborty, I.; Saha, A.; Kurkute, P.; Ghosh, S. Dual Functionalized Graphene Oxide Serves as a Carrier for Delivering Oligohistidine- and Biotin-Tagged Biomolecules into Cells. *Macromol. Biosci.* **2013**, *13*, 1478–1484.
(52) Majzoub, R. N.; Chan, C.-L.; Ewert, K. K.; Silva, B. F. B.; Liang, K. S.; Jacovetty, E. L.; Carragher, B.; Potter, C. S.; Safinya, C. R. Uptake and Transfection Efficiency of PEGylated Cationic Liposome-DNA Complexes with and without RGD-Tagging. *Biomaterials* **2014**, *35*, 4996–5005.
(53) Cardoso, A.; Trabulo, S.; Moreira, J. N.; Duzgunes, N.; de Lima, M. C. P. Targeted Lipoplexes for siRNA Delivery. *Methods Enzymol.* **2009**, *465*, 267–287.
(54) Zhu, L.; Mahato, R. I. Lipid and Polymeric Carrier-Mediated Nucleic Acid Delivery. *Expert Opin. Drug Deliv.* **2010**, *7*, 1209–1226.
(55) Shirazi, R. S.; Ewert, K. K.; Leal, C.; Majzoub, R. N.; Bouxsein, N. F.; Safinya, C. R. Synthesis and Characterization of Degradable Multivalent Cationic Lipids with Disulfide-Bond Spacers for Gene Delivery. *Biochim. Biophys. Acta* **2011**, *1808*, 2156–2166.
(56) Chan, C.-L.; Majzoub, R. N.; Shirazi, R. S.; Ewert, K. K.; Chen, Y.-J.; Liang, K. S.; Safinya, C. R. Endosomal Escape and Transfection Efficiency of PEGylated Cationic Liposome-DNA Complexes Prepared with an Acid-Labile PEG-Lipid. *Biomaterials* **2012**, *33*, 4928–4935.
(57) Doherty, G. J.; McMahon, H. T. Mechanisms of Endocytosis. *Annu. Rev. Biochem.* **2009**, *78*, 857–902.
(58) Stenmark, H. Rab GTPases as Coordinators of Vesicle Traffic. *Nat. Rev. Mol. Cell Biol.* **2009**, *10*, 513–525.
(59) Zerial, M.; Mcbride, H. Rab Proteins As Membrane Organizers. *Nat. Rev. Mol. Cell Biol.* **2001**, *2*, 107–117.
(60) Sonnichsen, B.; De Renzis, S.; Nielsen, E.; Rietdorf, J.; Zerial, M. Distinct Membrane Domains on Endosomes in the Recycling Pathway Visualized by Multicolor Imaging of Rab4, Rab5, and Rab11. *J. Cell Biol.* **2000**, *149*, 901–914.
(61) Yamashiro, D. J.; Tycko, B.; Fluss, S. R.; Maxfield, F. R. Segregation of Transferrin to a Mildly Acidic (pH 6.5) Para-Golgi Compartment in the Recycling Pathway. *Cell* **1984**, *37*, 789–800.
(62) Grant, B. D.; Donaldson, J. G. Pathways and Mechanisms of Endocytic Recycling. *Nat. Rev. Mol. Cell Biol.* **2009**, *10*, 597–608.
(63) Ullrich, O.; Reinsch, S.; Urbé, S.; Zerial, M.; Parton, R. G. Rab11 Regulates Recycling through the Pericentriolar Recycling Endosome. *J. Cell Biol.* **1996**, *135*, 913–924.
(64) Rink, J.; Ghigo, E.; Kalaidzidis, Y.; Zerial, M. Rab Conversion as a Mechanism of Progression from Early to Late Endosomes. *Cell* **2005**, *122*, 735–749.
(65) Piper, R. C.; Katzmann, D. J. Biogenesis and Function of Multivesicular Bodies. *Annu. Rev. Cell Dev. Biol.* **2007**, *23*, 519–547.
(66) Bucci, C.; Thomsen, P.; Nicoziani, P.; McCarthy, J.; van Deurs, B. Rab7: A Key to Lysosome Biogenesis. *Mol. Biol. Cell* **2000**, *11*, 467–480.
(67) Kowal, J.; Tkach, M.; Théry, C. Biogenesis and Secretion of Exosomes. *Curr. Opin. Cell Biol.* **2014**, *29*, 116–125.
(68) Majzoub, R. N.; Chan, C. L.; Ewert, K. K.; Silva, B. F. B.; Liang, K. S.; Safinya, C. R. Fluorescence Microscopy Colocalization of Lipid-Nucleic Acid Nanoparticles with Wildtype and Mutant Rab5-GFP: A Platform for Investigating Early Endosomal Events. *Biochim. Biophys. Acta - Biomembr.* **2015**, *1848*, 1308–1318.

(69) Gilleron, J.; Querbes, W.; Zeigerer, A.; Borodovsky, A.; Marsico, G.; Schubert, U.; Manygoats, K.; Seifert, S.; Andree, C.; Stöter, M.; et al. Image-Based Analysis of Lipid Nanoparticle-Mediated siRNA Delivery, Intracellular Trafficking and Endosomal Escape. *Nat. Biotechnol.* **2013**, *31*, 638–646.

(70) Rehman, Z.; Hoekstra, D.; Zuhorn, I. S. Protein Kinase A Inhibition Modulates the Intracellular Routing of Gene Delivery Vehicles in HeLa Cells, Leading to Productive Transfection. *J. Control. Release* **2011**, *156*, 76–84.

(71) Georgieva, J. V; Kalicharan, D.; Couraud, P.-O.; Romero, I. a; Weksler, B.; Hoekstra, D.; Zuhorn, I. S. Surface Characteristics of Nanoparticles Determine Their Intracellular Fate in and Processing by Human Blood-Brain Barrier Endothelial Cells in Vitro. *Mol. Ther.* **2011**, *19*, 318–325.

(72) Akita, H.; Ito, R.; Khalil, I. a.; Futaki, S.; Harashima, H. Quantitative Three-Dimensional Analysis of the Intracellular Trafficking of Plasmid DNA Transfected by a Nonviral Gene Delivery System Using Confocal Laser Scanning Microscopy. *Mol. Ther.* **2004**, *9*, 443–451.

(73) Hama, S.; Akita, H.; Ito, R.; Mizuguchi, H.; Hayakawa, T.; Harashima, H. Quantitative Comparison of Intracellular Trafficking and Nuclear Transcription between Adenoviral and Lipoplex Systems. *Mol. Ther.* **2006**, *13*, 786–794.

(74) Missirlis, D.; Teesalu, T.; Black, M.; Tirrell, M. The Non-Peptidic Part Determines the Internalization Mechanism and Intracellular Trafficking of Peptide Amphiphiles. *PLoS One* **2013**, *8*, e54611.

(75) Sahay, G.; Querbes, W.; Alabi, C.; Eltoukhy, A.; Sarkar, S.; Zurenko, C.; Karagiannis, E.; Love, K.; Chen, D.; Zoncu, R.; et al. Efficiency of siRNA Delivery by Lipid Nanoparticles Is Limited by Endocytic Recycling. *Nat. Biotechnol.* **2013**, *31*, 653–658.

(76) Ewert, K. K.; Kotamraju, V. R.; Majzoub, R. N.; Steffes, V. M.; Wonder, E. A.; Teesalu, T.; Ruoslahti, E.; Safinya, C. R. Synthesis of Linear and Cyclic peptide–PEG–lipids for Stabilization and Targeting of Cationic liposome–DNA Complexes. *Bioorg. Med. Chem. Lett.* **2016**, *26*, 1618–1623.

(77) Majzoub, R. N.; Ewert, K. K.; Jacovetty, E. L.; Carragher, B.; Potter, C. S.; Li, Y.; Safinya, C. R. Patterned Threadlike Micelles and DNA-Tethered Nanoparticles: A Structural Study of PEGylated Cationic Liposome-DNA Assemblies. *Langmuir* **2015**, *31*, 7073–7083.

(78) Teesalu, T.; Sugahara, K. N.; Kotamraju, V. R.; Ruoslahti, E. C-End Rule Peptides Mediate Neuropilin-1-Dependent Cell, Vascular, and Tissue Penetration. *Proc. Natl. Acad. Sci. U. S. A.* **2009**, *106*, 16157–16162.

(79) Pang, H.-B.; Braun, G. B.; Friman, T.; Aza-Blanc, P.; Ruidiaz, M. E.; Sugahara, K. N.; Teesalu, T.; Ruoslahti, E. An Endocytosis Pathway Initiated through Neuropilin-1 and Regulated by Nutrient Availability. *Nat. Commun.* **2014**, *5*, 4904.

(80) Roth, L.; Agemy, L.; Kotamraju, V. R.; Braun, G.; Teesalu, T.; Sugahara, K. N.; Hamzah, J.; Ruoslahti, E. Transtumoral Targeting Enabled by a Novel Neuropilin-Binding Peptide. *Oncogene* **2012**, *31*, 3754–3763.

(81) Saha, A.; Mohapatra, S.; Kurkute, P.; Jana, B.; Sarkar, J.; Mondal, P.; Ghosh, S. Targeted Delivery of a Novel Peptide–docetaxel Conjugate to MCF-7 Cells through Neuropilin-1 Receptor: Reduced Toxicity and Enhanced Efficacy of Docetaxel. *RSC Adv.* **2015**, *5*, 92596–92601.

(82) Sugahara, K. N.; Teesalu, T.; Karmali, P. P.; Kotamraju, V. R.; Agemy, L.; Girard, O. M.;

Hanahan, D.; Mattrey, R. F.; Ruoslahti, E. Tissue-Penetrating Delivery of Compounds and Nanoparticles into Tumors. *Cancer Cell* **2009**, *16*, 510–520.

(83) Soker, S.; Takashima, S.; Miao, H. Q.; Neufeld, G.; Klagsbrun, M. Neuropilin-1 Is Expressed by Endothelial and Tumor Cells as an Isoform-Specific Receptor for Vascular Endothelial Growth Factor. *Cell* **1998**, *92*, 735–745.

(84) Varner, J. A.; Cheresh, D. A. Integrins and Cancer. *Current Opinion in Cell Biology*. 1996, pp 724–730.

(85) Lee, Y.-C.; Jin, J.-K.; Cheng, C.-J.; Huang, C.-F.; Song, J. H.; Huang, M.; Brown, W. S.; Zhang, S.; Yu-Lee, L.-Y.; Yeh, E. T.; et al. Targeting Constitutively Activated β1 Integrins Inhibits Prostate Cancer Metastasis. *Mol. Cancer Res.* **2013**, *11*, 405–417.

(86) Bouxsein, N. F.; McAllister, C. S.; Ewert, K. K.; Samuel, C. E.; Safinya, C. R. Structure and Gene Silencing Activities of Monovalent and Pentavalent Cationic Lipid Vectors Complexed with siRNA. *Biochemistry* **2007**, *46*, 4785–4792.

(87) Chan, C.-L.; Ewert, K. K.; Majzoub, R. N.; Hwu, Y.-K.; Liang, K. S.; Leal, C.; Safinya, C. R. Optimizing Cationic and Neutral Lipids for Efficient Gene Delivery at High Serum Content. *J. Gene Med.* **2014**, *16*, 84–96.

(88) Ewert, K.; Ahmad, A.; Evans, H. M.; Schmidt, H. W.; Safinya, C. R. Efficient Synthesis and Cell-Transfection Properties of a New Multivalent Cationic Lipid for Nonviral Gene Delivery. *J. Med. Chem.* **2002**, *45*, 5023–5029.

(89) Sun, Q.; Westphal, W.; Wong, K. N.; Tan, I.; Zhong, Q. Rubicon Controls Endosome Maturation as a Rab7 Effector. *Proc. Natl. Acad. Sci. U. S. A.* **2010**, *107*, 19338–19343.

(90) Choudhury, A.; Dominguez, M.; Puri, V.; Sharma, D. K.; Narita, K.; Wheatley, C. L.; Marks, D. L.; Pagano, R. E. Rab Proteins Mediate Golgi Transport of Caveola-Internalized Glycosphingolipids and Correct Lipid Trafficking in Niemann-Pick C Cells. *J. Clin. Invest.* **2002**, *109*, 1541–1550.

(91) Silva, B. F. B.; Majzoub, R. N.; Chan, C. L.; Li, Y.; Olsson, U.; Safinya, C. R. PEGylated Cationic Liposome-DNA Complexation in Brine Is Pathway-Dependent. *Biochim. Biophys. Acta - Biomembr.* **2014**, *1838*, 398–412.

(92) Majzoub, R. N.; Ewert, K. K.; Safinya, C. R. Quantitative Intracellular Localization of Cationic Lipid-Nucleic Acid Nanoparticles with Fluorescence Microscopy. In *Non-Viral Gene Delivery Vectors: Methods and Protocols*; Candiani, G., Ed.; Springer/Humana Press: Totowa, NJ, 2016; In press.

(93) Majzoub, R. N. Investigating Intracellular Pathways of Surface-Functionalized Cationic Lipid-DNA Nanoparticles Using Quantitative Fluorescence Microscopy. Ph.D. Dissertation, University of California, Santa Barbara, CA, 2015.

(94) Crocker, J.; Crocker, J.; Grier, D. Methods of Digital Video Microscopy for Colloidal Studies. *J. Colloid Interface Sci.* **1996**, *179*, 298–310.

(95) Lodish, H.; Berk, A.; Zipursky, S. L.; Matsudaira, P.; Baltimore, D.; Darnell, J. Section 17.9, Receptor-Mediated Endocytosis and the Sorting of Internalized Proteins. In *Molecular Cell Biology*; W. H. Freeman: New York, 2000.

Figure Captions

Figure 1. Liposomes as drug and gene delivery vectors. (A) A liposome, a self-assembled spherical shell of amphiphilic lipid molecules, containing hydrophobic molecules (red spheres) trapped within the bilayer. Liposomes can be used as drug delivery vehicles by trapping hydrophobic drugs within the oily membrane or hydrophilic drugs within the aqueous lumen. (B) A surface-modified liposome with polymer-lipid molecules forming a polymer corona. Surface properties of the liposomes can be optimized for *in vivo* delivery using hydrophilic polymers (e.g., poly(ethylene glycol), PEG). These polymers provide steric repulsion that inhibits nonspecific protein binding and opsonization by the immune system, resulting in "stealth" particles. Targeted delivery can also be achieved by the addition of cell-targeting ligands (white rectangles) to the distal end of the polymer-lipid. (C) A complex of cationic lipid bilayers with negatively charged nucleic acids (purple rods) in a lamellar liquid crystal structure. These complexes are used as gene delivery vectors due to their ability to condense nucleic acids into nanostructured particles. These complexes can be further optimized by the addition of polymer-lipids, which stabilize the complex into a nanoparticle of well-defined size. Acid-labile polymer-lipids release the polymer in low-pH late endosomes, promoting interactions between cell and nanoparticle membranes. Adapted and modified with permission from [ref. 3].

Figure 2. The endosomal recycling and late endosome/lysosome pathways. Upon internalization of cargo via macropinocytic ruffles (MPR) or clathrin pits (CP), the cargo is trafficked in macropinosomes (MP) or clathrin-coated vesicles (CCV). The MP and CCV undergo Rab5-mediated fusion to form the early endosome (EE). From the early endosome, cargo can be sequestered into vesicles which pinch off and either traffic to the perinuclear recycling center (PRC) or the plasma membrane (PM). From the PRC, cargo is trafficked to the plasma membrane via recycling endosomes (RE) containing Rab11 (green). Alternatively, after sufficient time has elapsed, the EE will gradually lose Rab5 (orange) and acquire Rab7 (purple), marking its evolution into a late endosome/multivesicular body (LE/MVB). The LE/MVB contains an acidic lumen (pink) and both Rab7 and Rab9 (light blue) on its surface. In some cases, LE/MVB will fuse with the plasma membrane, releasing the intraluminal vesicles as exosomes. Rab7 mediates fusion between lysosomes and LE/MVB to form a hybrid lyso-endosome containing characteristics of both organelles. Eventually the lyso-endosome will mature into a lysosome. Rab9 is also associated with transport of the mannose-6-phosphate receptor from the late endosome to the trans-Golgi Network (TGN).

Figure 3. Schematics and corresponding legend showing the compositions of nanoparticles (NPs). All NPs were prepared at $\rho_{chg} = 5$. NPs 1–3, 4–6, and 7–9 were formulated at the molar ratios 10/80/10, 50/40/10, and 70/20/10 of MVL5/DOPC/x, respectively, with x = PEG-lipid (NP1, NP4, NP7), RGD-PEG-lipid (NP2, NP5, NP8), or RPARPAR-PEG-lipid (NP3, NP6, NP9).

Figure 4. Transfection efficiency versus cationic lipid content for CL–DNA nanoparticles containing MVL5. The transfection efficiency (TE) of nanoparticles containing MVL5/DOPC/PEG2K-lipid (orange), MVL5/DOPC/RGD-PEG2K-lipid (purple), MVL5/DOPC/RPARPAR-PEG2K-lipid (green) generally increases with membrane charge density. For very high membrane charge density RGD-PEG2K-lipid NPs, TE decreases slightly. At all charge densities, the transfection of RGD-PEG-lipid-containing NPs is the highest, followed by the control PEG-lipid NPs. NPs containing RPARPAR-PEG-lipid had the lowest TE at every charge density examined in this study. All CL–DNA NPs (NP1–9) performed better than naked DNA and worse than Lipofectamine 2000 (a commercial *in vitro* transfection agent).

Figure 5. Multi-organelle colocalization using Rab GTPases and Lysotracker. Lysotracker Red, a membrane permeable small molecule dye, labels acidic organelles. In the micrographs, Rab-GFP is shown in green, Lysotracker in red, with overlap appearing yellow. (A, B) Rab5 and Rab11 label early and recycling endosomes, respectively, both of which show low levels of colocalization with Lysotracker Red. (C) Rab7, a marker for late endosomes and lysosomes shows high levels of colocalization with Lysotracker. (D) Rab9, a marker of late endosomes and vesicles that traffic between late endosomes and the Golgi apparatus, shows moderate levels of colocalization with Lysotracker. (E) Quantitative colocalization results showing the total number of Rab-labeled vesicles per cell (total height of bar) and the fraction of the Rab-labeled vesicles that colocalize with Lyostracker Red (yellow portion).

Figure 6. CL–DNA NPs traffic through both recycling and late endosome/lysosome pathways. (A, B, C) Fluorescence micrograph and cropped regions of fixed PC-3 cells expressing Rab11-GFP (green), treated with Lysotracker Red (red) and incubated with 10/80/10 MVL5/DOPC/RPARPAR-PEG-lipid CL–DNA NPs (blue) at ρ_{chg} =5 for 5 hours. The inset displays the brightfield micrograph of the cells. (D, E, F) show the individual channels from (C) for clarity. (G, H) Intensity profiles of the dashed lines in (B) and (C). In (B) and (G), an acidic organelle (i) and a recycling endosome (ii), each containing an NP, are shown. In (C, D, E, F, H) the perinuclear recycling center (green arrow), a large, bright resolvable signal in the green channel, is shown containing an NP (solid blue blue). An acidic organelle containing a NP is also shown (red arrow, broken blue arrow). Scales bars in (A) and (B,C) are 10 μm and 5 μm, respectively.

Figure 7. Low membrane charge density CL–DNA NPs show high colocalization with Rab11-GFP. Low membrane charge density NPs were formulated with 10/80/10 MVL5/DOPC/x at ρ_{chg} = 5 where x = PEG-lipid (NP1), RGD-PEG-lipid (NP2), or RPARPAR-PEG-lipid (NP3) (see Figure 2). (A,B,C) Fluorescence micrographs and brightfield images (insets) of fixed PC-3 cells expressing Rab11-GFP (green) and treated with Lysotracker (red) such that acidic organelles (i.e., late endosomes and lysosomes) are visible. The cells have been incubated with

fluorescently-labeled nanoparticles of formulations NP1, NP2, and NP3, respectively (blue). (D) Simultaneous quantitative colocalization of NPs with recycling endosomes (green) and acidic organelles (red) for the NP compositions NP1, NP2, and NP3. In all three cases, NPs show colocalization with both markers. The use of linear RGD- or RPARPAR-PEG-lipid increases total uptake relative to the PEG-lipid control (compare the total height of the bars). The error for colocalization percentages is about ±2%. (E,F,G,H,I,J) Magnified boxed regions from (A,B,C) and intensity profiles. Examples of NP–Rab11 and NP–Lysotracker colocalization are marked with roman numerals and observed in all cases. Scale bars in (A,B,C) and (E,F,G) are 10 and 5 μm, respectively.

Figure 8. High membrane charge density CL–DNA NPs show comparable colocalization with Rab11-GFP and Lysotracker. High membrane charge density NPs were formulated with 50/40/10 MVL5/DOPC/x at ρ_{chg} = 5 where x = PEG-lipid (NP4), RGD-PEG-lipid (NP5), or RPARPAR-PEG-lipid (NP6) (see Figure 2). (A,B,C) Fluorescence micrographs and brightfield images (insets) of fixed PC-3 cells expressing Rab11-GFP (green) and treated with Lysotracker (red) such that acidic organelles (e.g., late endosomes and lysosomes) are visible. The cells have been incubated with fluorescently-labeled nanoparticles of formulations NP4, NP5, and NP6, respectively (blue). (D) Simultaneous quantitative colocalization of NPs with recycling endosomes (green) and acidic organelle (red) for the NP compositions NP4, NP5, and NP6. In all three cases, NPs show colocalization with both markers. The use of linear RGD- or RPARPAR-PEG-lipid has no effect on total uptake relative to the PEG-lipid control (compare the total height of the bars). The error for colocalization percentages is about ±2%. (E,F,G,H,I,J) Magnified boxed regions from (A,B,C) and intensity profiles. Examples of NP–Rab11 and NP–Lysotracker colocalization are marked with roman numerals and observed in all cases. Scale bars in (A,B,C) and (E,F,G) are 10 and 5 μm, respectively.

Figure 9. Very high membrane charge density CL–DNA NPs show high colocalization with Lysotracker. Very high membrane charge density NPs were formulated with 70/40/10 MVL5/DOPC/x at ρ_{chg} = 5 where x = PEG-lipid (NP7), RGD-PEG-lipid (NP8), or RPARPAR-PEG-lipid (NP9) (see Figure 2). (A,B,C) Fluorescence micrographs and brightfield images (insets) of fixed PC-3 cells expressing Rab11-GFP (green) and treated with Lysotracker (red) such that acidic organelles (e.g., late endosomes and lysosomes) are visible. The cells have been incubated with fluorescently-labeled nanoparticles of formulations NP7, NP8, and NP9, respectively (blue). (D) Simultaneous quantitative colocalization of NPs with recycling endosomes (green) and acidic organelle (red) for the NP compositions NP7, NP8, and NP9. In all three cases, NPs show colocalization with both markers. Total uptake was highest in the PEG-lipid control, decreasing with the use of RGD-PEG-lipid and RPARPAR-PEG-lipid (compare the total height of the bars). The error for colocalization percentages is about ±2%. (E,F,G,H,I,J) Magnified boxed regions from (A,B,C) and intensity profiles. Examples of NP–Rab11 and NP–

Lysotracker colocalization are marked with roman numerals and observed in all cases. Scale bars in (A,B,C) and (E,F,G) are 10 and 5 μm, respectively.

Figure 10. Comparison of the colocalization of nanoparticles with endosomal markers. The percentages of NPs showing colocalization with Rab11 (top) and Lysotracker (bottom) were extracted from figures 7D, 8D, and 9D for control PEG-lipid NPs (orange), RGD-PEG-lipid NPs (purple), and RPARPAR-PEG-lipid NPs (green). Rab11 colocalization varies little with charge density for the control PEG-lipid NPs. Both RGD- and RPARPAR-PEG-lipid NPs show a decrease in Rab11 colocalization from low to high charge density and little change from high to very high charge density. The control PEG-lipid NPs show a monotonic increase in Lysotracker colocalization with charge density. Both RGD- and RPARPAR-PEG-lipid NPs show a large increase in Lysotracker colocalization from low to high charge density and a smaller decrease from high to very high charge density. RPARPAR-PEG-lipid shows a smaller range of colocalization with both Rab11 and Lysotracker compared to RGD-PEG-lipid.

Figure 11. Correlation of transfection efficiency (TE) with endosomal marker colocalization. Transfection efficiency (TE) of control PEG-lipid NPs (orange), RGD-PEG-lipid NPs (purple), and RPARPAR-PEG-lipid NPs (green) is plotted against colocalization with Rab11 (A) and Lysotracker (B) for all NP formulations. Rab11 colocalization shows an inverse correlation with TE, while Lysotracker colocalization shows a weaker direct correlation with TE. Gray lines are included as guides to the eye.

Figure 1

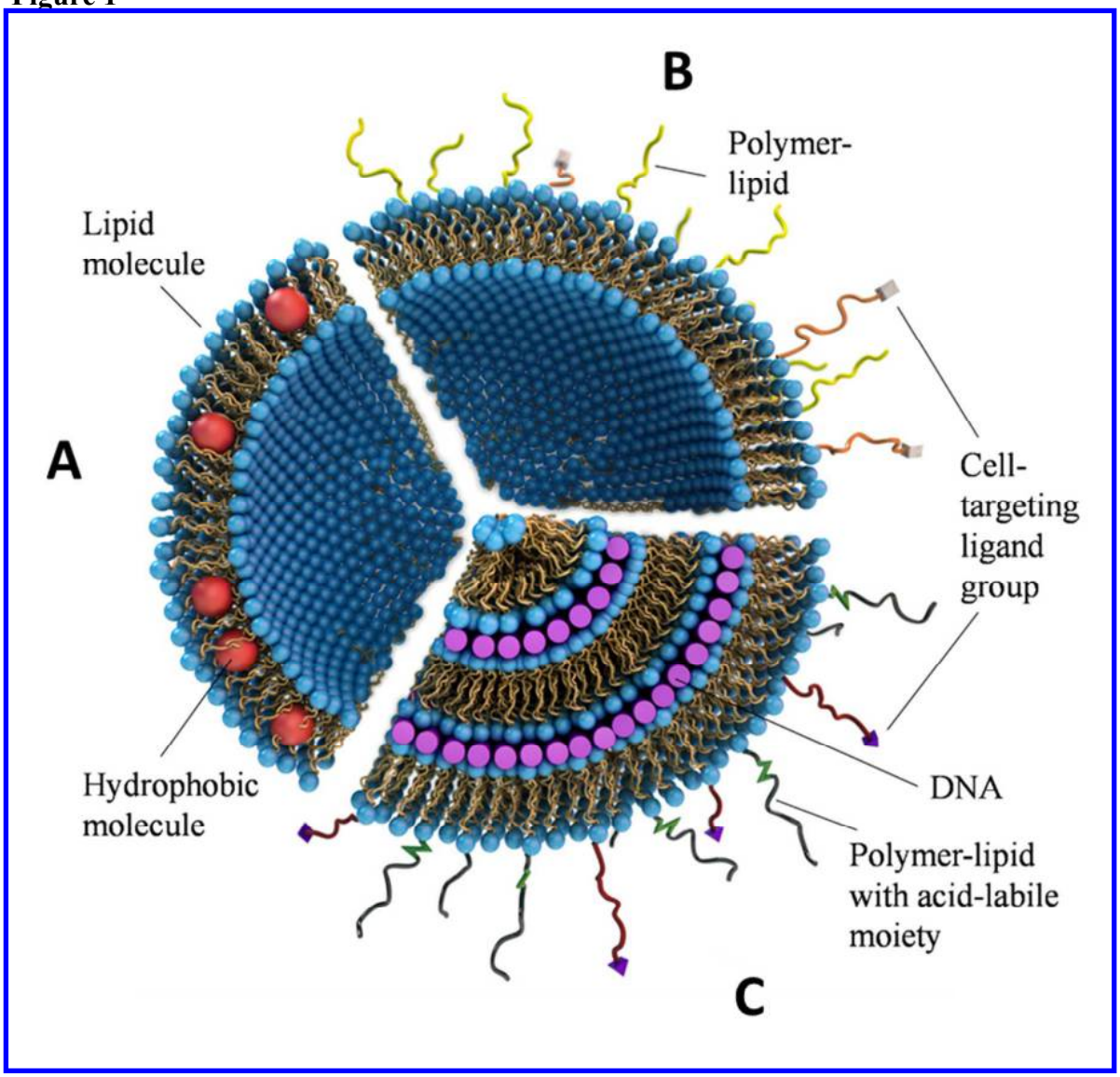
B
Polymer-
lipid
Lipid
molecule
A
Cell-
targeting
ligand
group
DNA
Hydrophobic
molecule
Polymer-lipid
with acid-labile
moiety
C

Figure 2

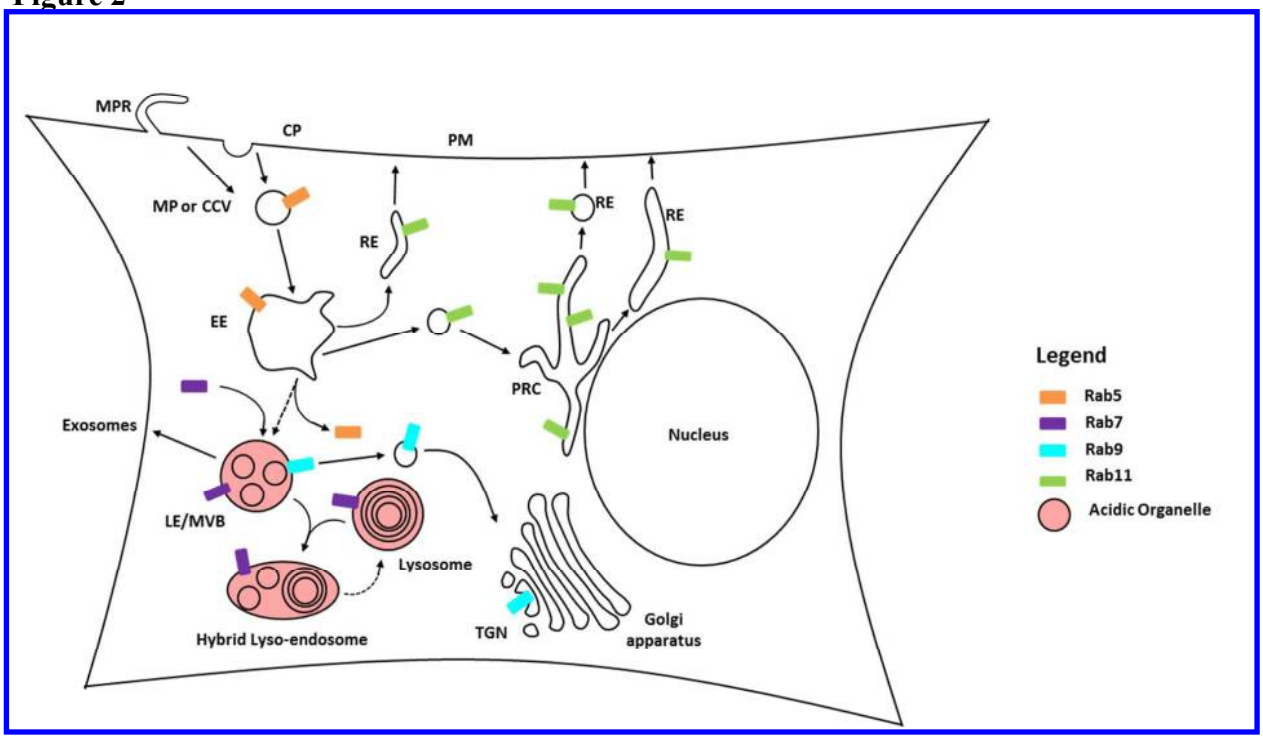
MPR
CP
PM
MP or CCV
RE
RE
RE
EE
PRC
Nucleus
Exosomes
LE/MVB
Lysosome
Hybrid Lyso-endosome
TGN
Golgi apparatus
Legend
Rab5
Rab7
Rab9
Rab11
Acidic Organelle

Figure 3

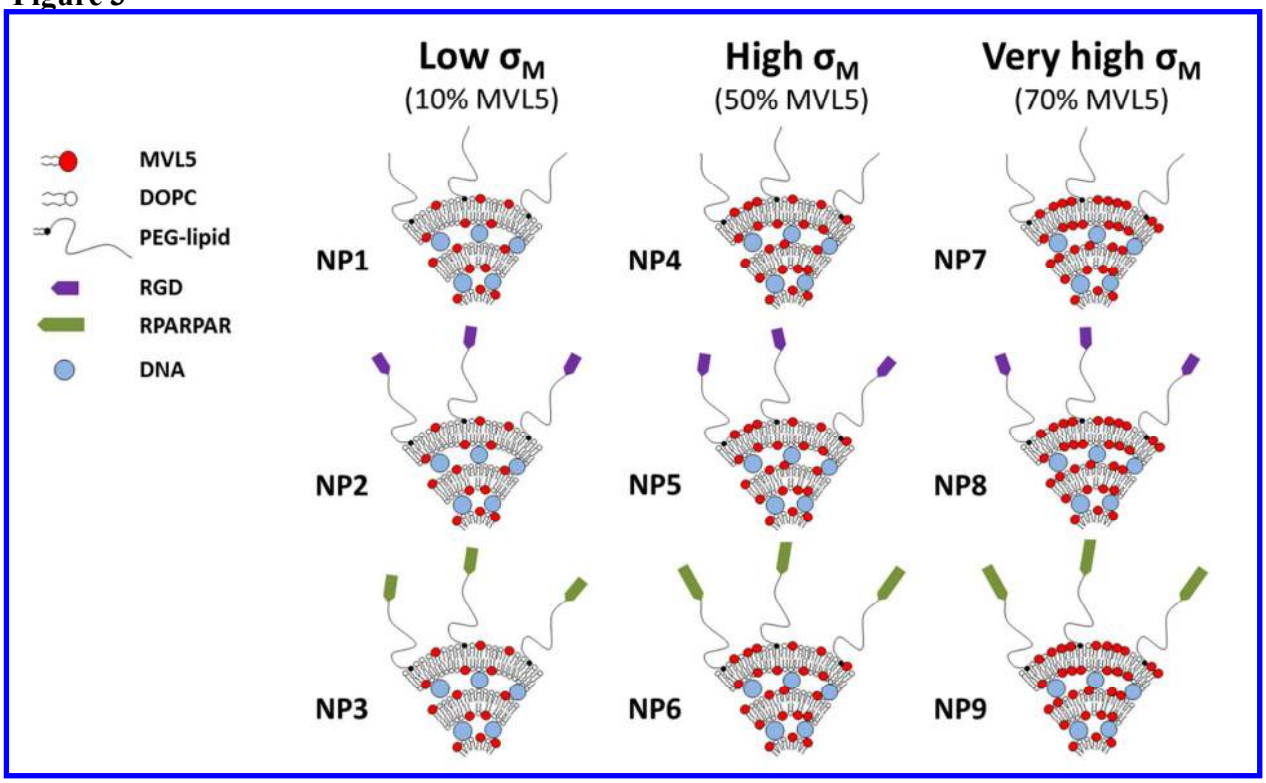
Low σ_M
(10% MVL5)
High σ_M
(50% MVL5)
Very high σ_M
(70% MVL5)
MVL5
DOPC
PEG-lipid
RGD
RPARPAR
DNA
NP1
NP2
NP3
NP4
NP5
NP6
NP7
NP8
NP9

Figure 4

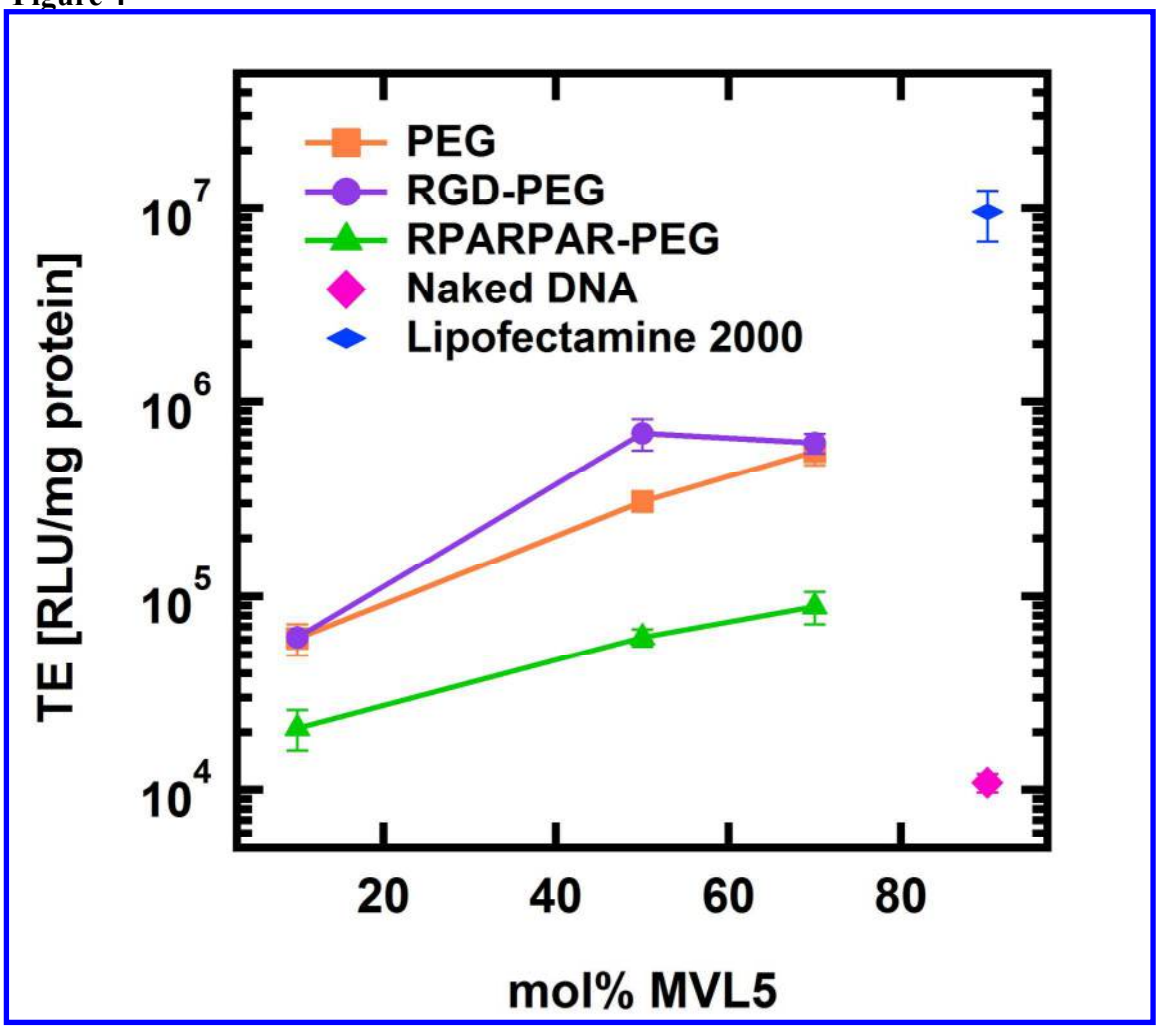
PEG
RGD-PEG
RPARPAR-PEG
Naked DNA
Lipofectamine 2000
TE [RLU/mg protein]
10^7
10^6
10^5
10^4
20
40
60
80
mol% MVL5

Figure 5

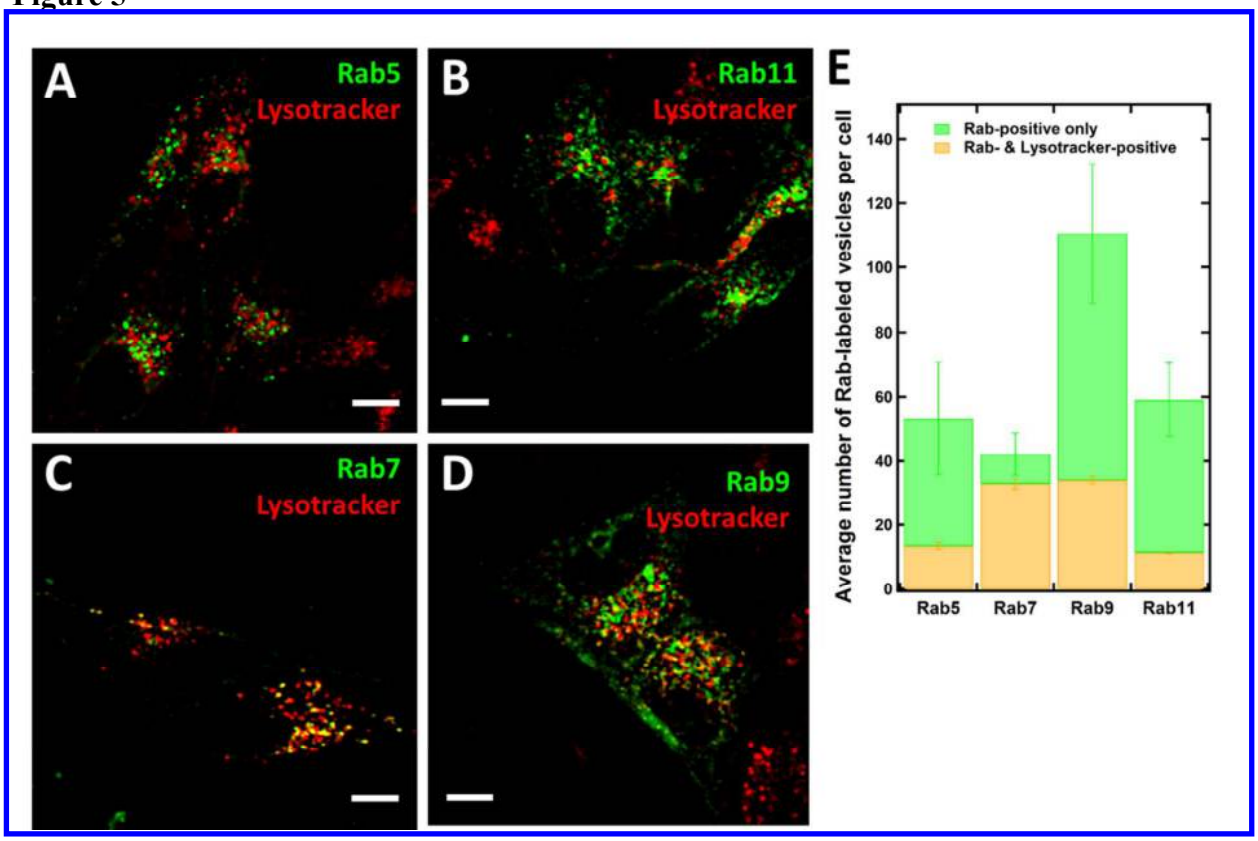
A
Rab5
Lysotracker
B
Rab11
Lysotracker
C
Rab7
Lysotracker
D
Rab9
Lysotracker
E
Rab-positive only
Rab- & Lysotracker-positive
Average number of Rab-labeled vesicles per cell
0
20
40
60
80
100
120
140
Rab5
Rab7
Rab9
Rab11

Figure 6

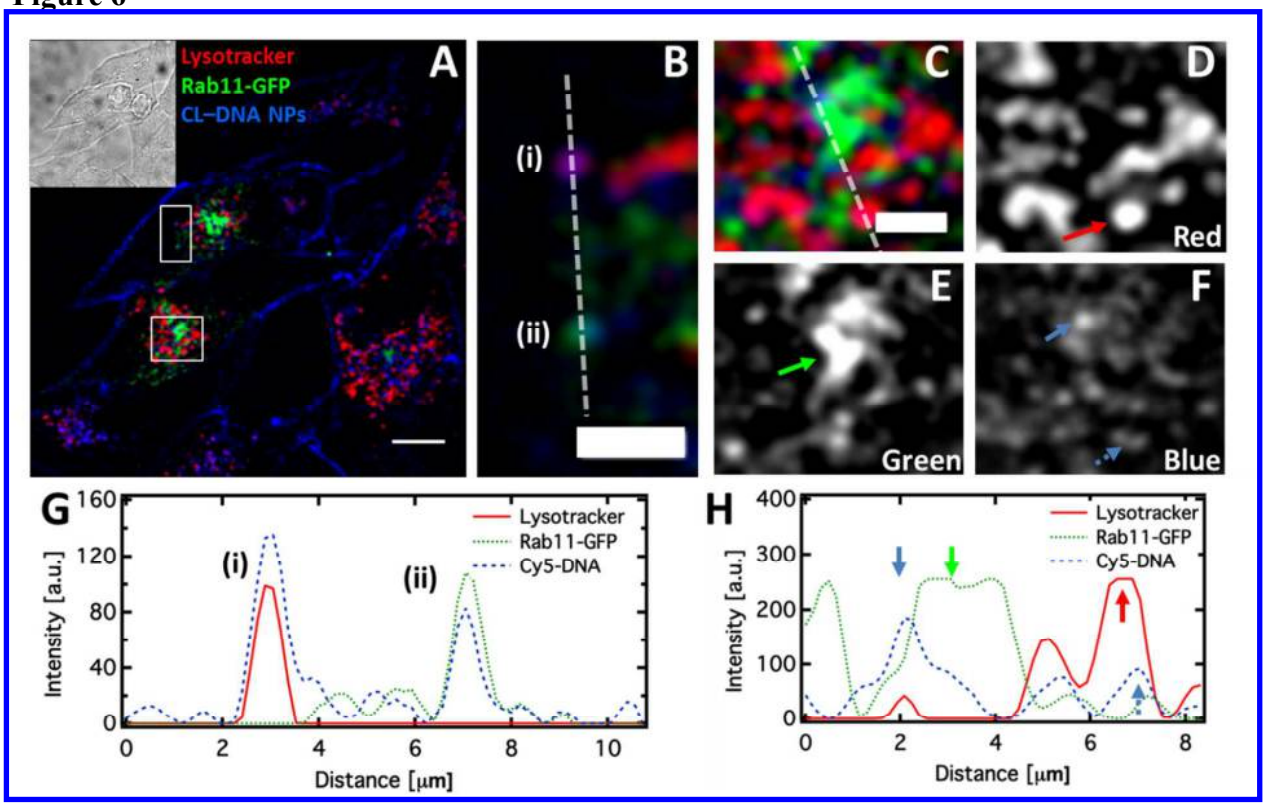
A
Lysotracker
Rab11-GFP
CL–DNA NPs
B
(i)
(ii)
C
D
Red
E
Green
F
Blue
G
Intensity [a.u.]
Distance [μm]
Lysotracker
Rab11-GFP
Cy5-DNA
(i)
(ii)
H
Intensity [a.u.]
Distance [μm]
Lysotracker
Rab11-GFP
Cy5-DNA

Figure 7

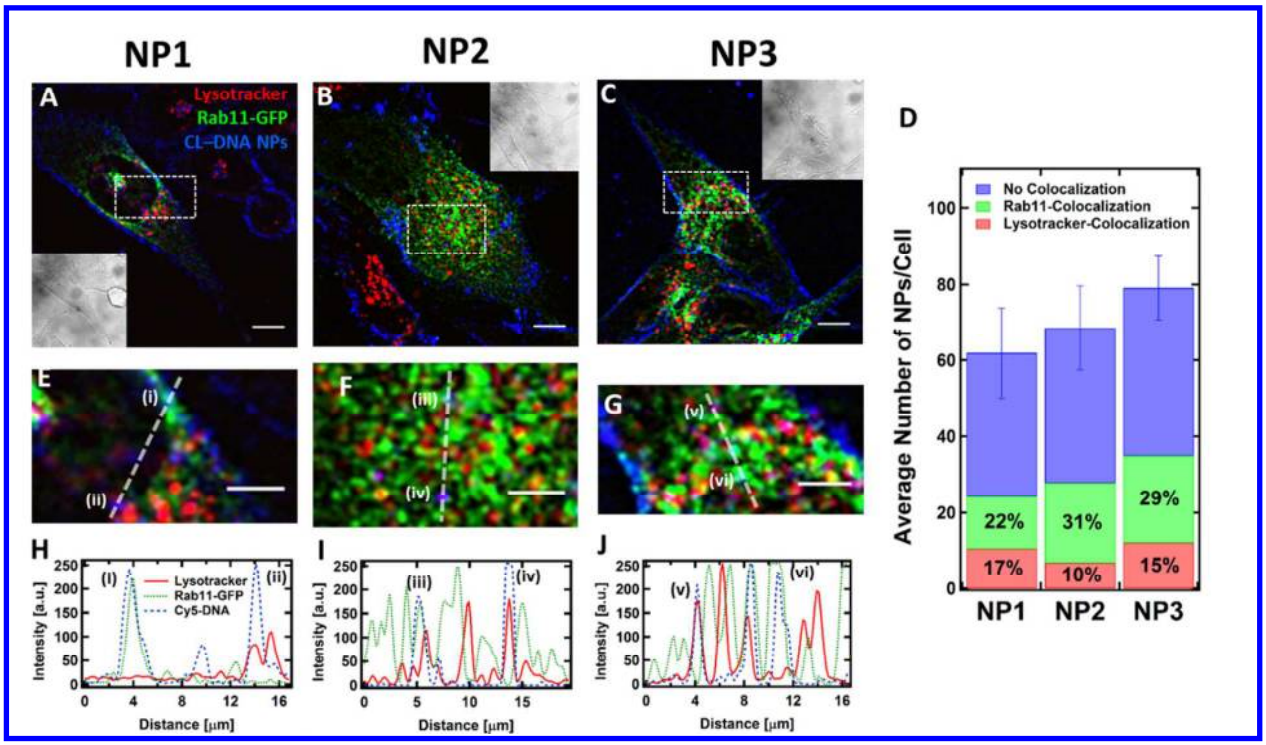
NP1
NP2
NP3
A
Lysotracker
Rab11-GFP
CL–DNA NPs
B
C
D
No Colocalization
Rab11-Colocalization
Lysotracker-Colocalization
Average Number of NPs/Cell
100
80
60
40
20
0
22%
31%
29%
17%
10%
15%
NP1
NP2
NP3
E
(i)
(ii)
F
(iii)
(iv)
G
(v)
(vi)
H
I
J
Lysotracker
Rab11-GFP
Cy5-DNA
Intensity [a.u.]
Distance [μm]

Figure 8

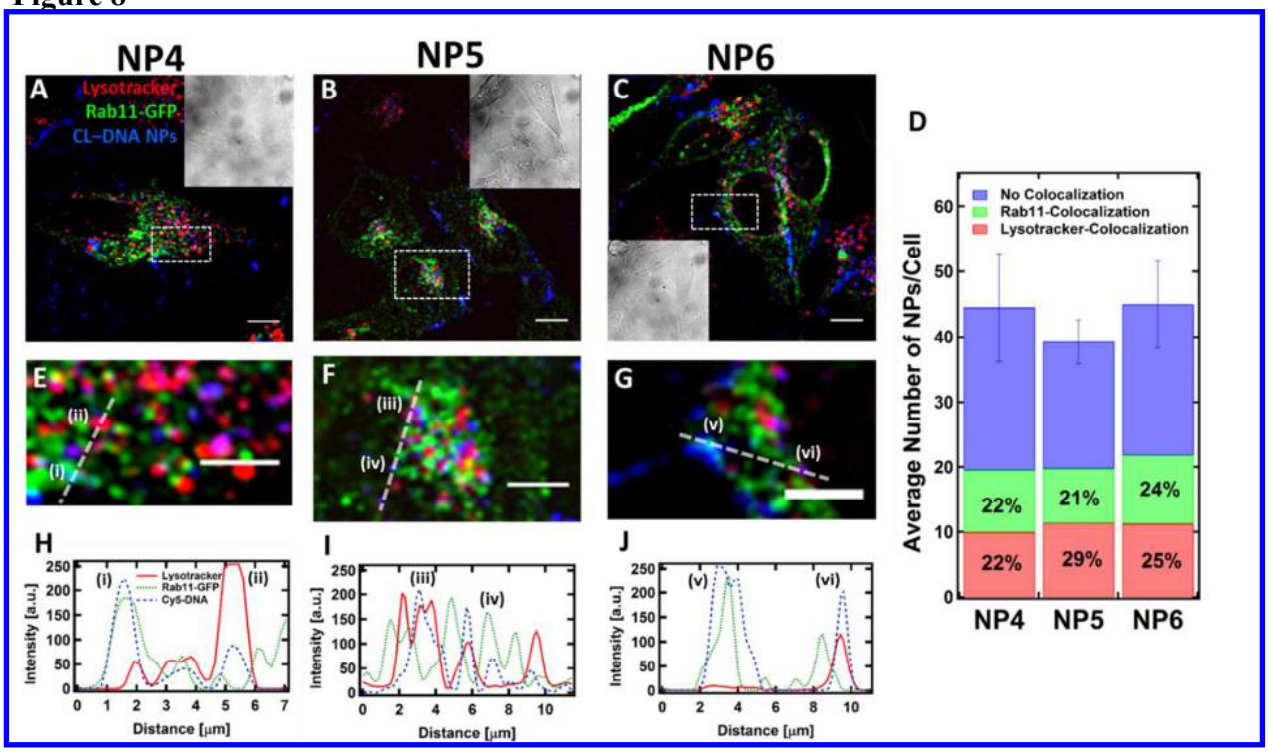
NP4
NP5
NP6
A
Lysotracker
Rab11-GFP
CL–DNA NPs
B
C
D
No Colocalization
Rab11-Colocalization
Lysotracker-Colocalization
Average Number of NPs/Cell
22%
22%
21%
29%
24%
25%
NP4
NP5
NP6
E
(i)
(ii)
F
(iii)
(iv)
G
(v)
(vi)
H
I
J
Lysotracker
Rab11-GFP
Cy5-DNA
Intensity [a.u.]
Distance [μm]

Figure 9

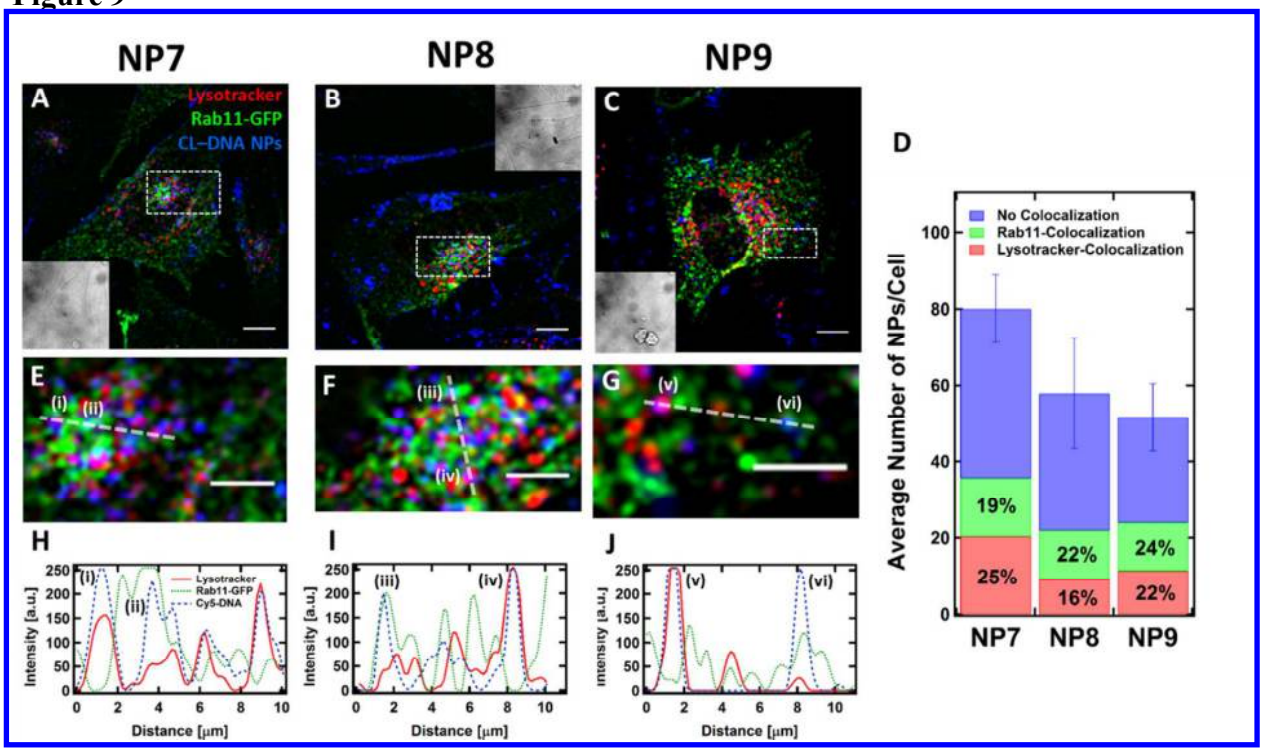
NP7
NP8
NP9
A
B
C
Lysotracker
Rab11-GFP
CL–DNA NPs
D
No Colocalization
Rab11-Colocalization
Lysotracker-Colocalization
Average Number of NPs/Cell
19%
25%
22%
16%
24%
22%
NP7
NP8
NP9
E
F
G
(i)
(ii)
(iii)
(iv)
(v)
(vi)
H
I
J
Lysotracker
Rab11-GFP
Cy5-DNA
Intensity [a.u.]
Distance [μm]

Figure 10

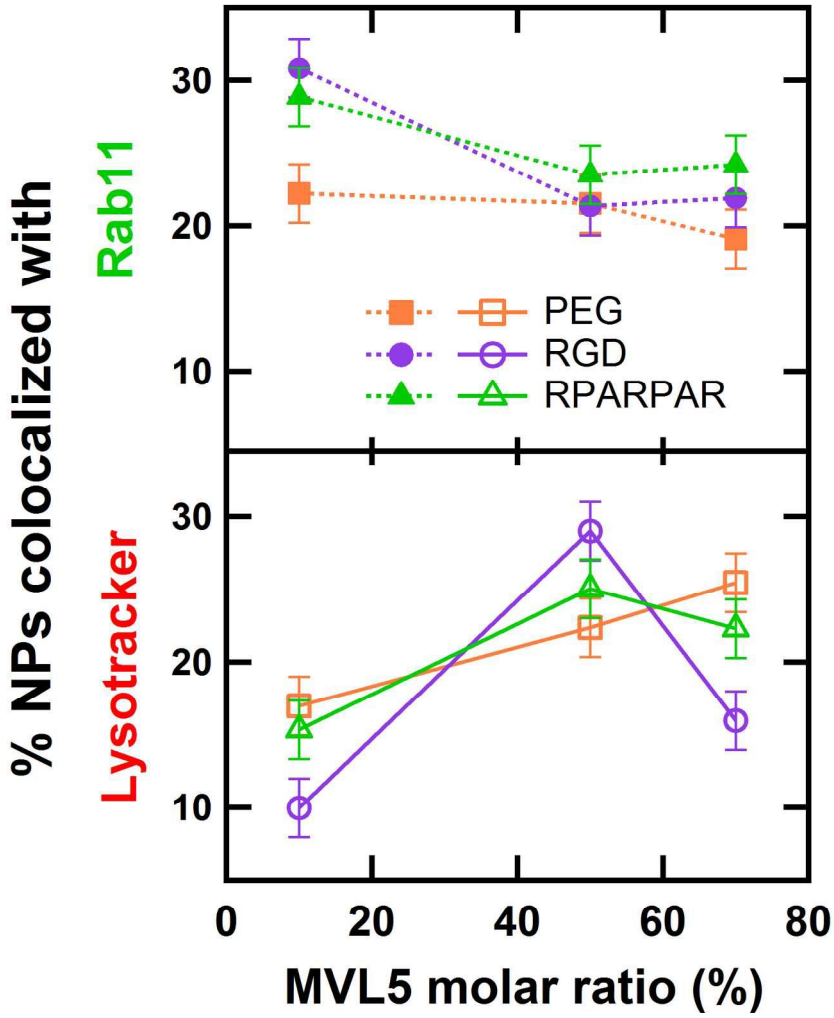
% NPs colocalized with
Rab11
Lysotracker
PEG
RGD
RPARPAR
30
20
10
30
20
10
0
20
40
60
80
MVL5 molar ratio (%)

Figure 11

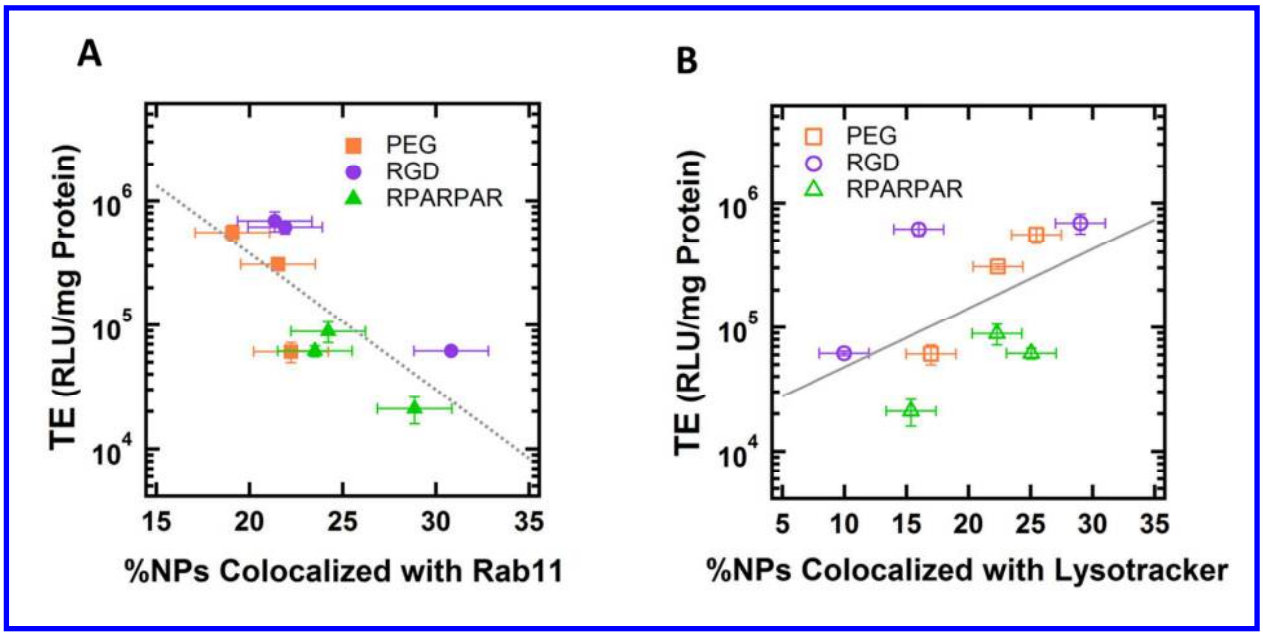
A
TE (RLU/mg Protein)
PEG
RGD
RPARPAR
%NPs Colocalized with Rab11
B
TE (RLU/mg Protein)
PEG
RGD
RPARPAR
%NPs Colocalized with Lysotracker

Table of Contents graphic